A Study of Convection Initiation in a Mesoscale Model Using High-Resolution Land Surface Initial Conditions

STANLEY B. TRIER, FEI CHEN, AND KEVIN W. MANNING

National Center for Atmospheric Research, Boulder, Colorado*

(Manuscript received 1 April 2004, in final form 9 July 2004)

ABSTRACT

A coupled convection-resolving mesoscale atmosphere–land surface model (LSM) is used to investigate land surface–planetary boundary layer (PBL) interactions responsible for the initiation of deep, moist convection over the southern Great Plains of the United States on 19 June 1998. A high-resolution land data assimilation system provides initial conditions to the LSM, facilitating examination of soil moisture effects on forecasts of deep convection.

During the late morning and early afternoon, the southwestern portion of a simulated southwest–northeast (SW–NE)-oriented surface water vapor gradient zone evolves into an intense dryline, unlike the northeastern portion, which remains relatively weak. Despite these regional differences, midafternoon convection initiation occurs within a ~100-km-wide region of enhanced PBL depth along much of the SW–NE extent of the water vapor gradient zone. The afternoon PBL depth maximum results from a midmorning-to-early afternoon surface sensible heat flux maximum of similar horizontal scale, and is reinforced by an ensuing mesoscale ($L \sim 100$ km) vertical circulation. Finescale ($L \sim 10$ km) PBL circulations that directly trigger deep convection are confined within this mesoscale region that contains the deeper and more unstable PBL.

Comparisons among different simulations reveal that thermodynamic stability and simulated convection initiation are affected by details in the initial soil moisture distribution, through differences in the partitioning of the surface heat and moisture fluxes. These differences in convection initiation among simulations occur despite only minor differences in the overall structure of the afternoon surface moisture gradient zone, which has potentially important implications for operational forecasts of deep convection.

1. Introduction

The diurnal cycle of surface heating and its destabilizing effects on the planetary boundary layer (PBL) are of primary importance to the development of deep, moist cumulus convection. Recent research has shown that land surface characteristics, including soil moisture and vegetation type can affect how solar radiation influences development of convective precipitation (see Pielke 2001 for a comprehensive review).

The influence of land surface–atmosphere interactions on initiation of deep, moist convection (hereafter referred to as simply convection initiation) results from a combination of related effects. First, the partition of surface heat and moisture flux that contributes to the growth and thermodynamic destabilization of the PBL is highly dependent on land surface characteristics. Second, horizontal gradients of PBL virtual potential temperature, θ_v, and PBL depth that result from differential heating over heterogeneous surfaces are associated with horizontal pressure gradients capable of generating mesoscale solenoidal circulations (e.g., Segal and Arritt 1992). Under hydrostatic conditions, the strength of the mesoscale circulation is proportional to the magnitude of the θ_v gradient on a horizontal surface and the depth through which it extends (Pielke and Segal 1986). These circulations may contribute to the reduction of convective inhibition (CIN; Colby 1984) beneath the level of free convection (LFC) and thus focus where convection initiation from additional lifting mechanisms can occur. In cases where such circulations are sufficiently persistent and intense, they may also directly trigger convection by locally saturating conditionally or potentially unstable lower-tropospheric layers.

Recent efforts that have coupled land surface models (LSMs) with mesoscale atmospheric models have permitted examination of land surface influences on convective precipitation in increasingly complex and realistic regional-scale environments. For instance, Chen et al. (2001) used a coupled LSM–mesoscale atmospheric model to demonstrate the importance of surface heterogeneities that resulted from forest fire activity on flood-producing convective rainfall in the Rocky Moun-

* The National Center for Atmospheric Research is sponsored by the National Science Foundation.

Corresponding author address: Dr. Stanley B. Trier, NCAR/MMM, P.O. Box 3000, Boulder, CO 80307-3000.
E-mail: trier@ucar.edu

tain foothills southwest of Denver, Colorado. In the present study, we use a coupled LSM–mesoscale atmospheric model initialized with output from a high-resolution land data assimilation system to examine influences of land surface–atmosphere interactions on convection initiation over the southern Great Plains (SGP) of the Untied States.

The warm-season SGP environment differs from that of the front range of the Rocky Mountains in several important ways. Unlike the sharp contrasts in terrain that occur over small horizontal distances in the Rocky Mountain region, the terrain of the SGP exhibits a gentle slope over a larger (i.e., regional) horizontal scale. The frequent juxtaposition of two disparate air masses including a warm, moist air mass originating from the Gulf of Mexico to the southeast, and a hot, dry air mass originating from the arid elevated plateau to the west and southwest results in large climatological differences in precipitation across the SGP. The horizontal gradients in seasonal and annual precipitation, in turn, support pronounced regional-scale longitudinal differences in land surface characteristics including soil moisture and vegetation patterns. Large contrasts in lower-tropospheric water vapor mixing ratio, q_v, are often found across the region in association with the juxtaposition of the different air masses.

Diurnally driven processes occurring during the spring and early summer can result in the afternoon intensification of the regional surface q_v gradient into a stronger finescale gradient ($|\nabla q_v| \sim 1$ g kg^{-1} km^{-1} over 10–15 km) referred to as the dryline (McGuire 1962). The dryline often serves as a focus for severe convection. Rhea (1966) noted that 60% of new radar echoes during a 3-yr period formed within 200 mi of the surface dryline. Hence, the diurnal cycle of the dryline and mechanisms governing its formation have been the focus of several decades of research. Results from numerous studies suggest that a combination of terrain effects, land surface processes, and environmental flow conditions influence its well-documented diurnal cycle (e.g., Schaefer 1974; Anthes et al. 1982; Benjamin 1986; Benjamin and Carlson 1986; Lanicci et al. 1987; Sun and Wu 1992; Ziegler et al. 1995; Shaw et al. 1997; Grasso 2000; Parsons et al. 2000; Peckham and Wicker 2000; Miller et al. 2001). Recent three-dimensional modeling studies with detailed representation of soil moisture and vegetation (Shaw et al. 1997; Grasso 2000) have demonstrated, in particular, the crucial role of soil moisture gradients in dryline formation.

The effects of land surface–atmosphere interactions on convection initiation near the surface water vapor gradient of the SGP have been less widely studied. Existing studies of dryline convection initiation have implicated the potential importance of motions on a variety of horizontal scales. These organized motions have ranged from the relatively weak, but areally extensive ($L \geq 100$ km), afternoon ''inland sea-breeze'' circulation initiated by differential heating along the sloped terrain of the SGP (e.g., Ogura and Chen 1977; Sun and Ogura 1979; Sun and Wu 1992) to more intense and concentrated ($L \sim 1$–10 km) PBL circulations that are responsible for the direct initiation of deep convection in both observational (e.g., Parsons et al. 1991; Atkins et al. 1998) and numerical (Ziegler et al. 1997) studies.

Our use of a mesoscale numerical model with convection-resolving resolution over a regional area allows us to elucidate the mechanisms by which land surface–atmosphere interactions contribute to the multiple scales of motion important to PBL-based convection initiation. The use of a high-resolution land surface data assimilation scheme also allows us to address practical questions concerning the potential impact of detailed soil moisture initial conditions on convection initiation in a numerical weather prediction (NWP) model.

The case selected for study occurred at the beginning of a 4-day period during which deep convection formed each afternoon along a quasi-stationary surface q_v gradient. Figure 1 illustrates the development of deep convection on 19 June 1998 from within preexisting shallow cumulus clouds situated along the major axis of the afternoon surface q_v gradient zone (Fig. 2a). This case occurred in weak midtropospheric flow devoid of large-amplitude transitory disturbances (Fig. 2b); a situation characteristic of the latter portion of the warm season. Although a weak midtropospheric wind and geopotential height disturbance in the vicinity of the surface q_v gradient in west Texas may have aided convection initiation, the SGP region (as a whole) evinces an anticyclonic tendency at midlevels with either neutral or weak geopotential height rises (Fig. 2b). One of the motivations for the selection of this particular case was the anticipation that land surface–atmosphere interactions would be easier to discern and potentially more important to convection initiation in an environment of weak synoptic forcing.

The remainder of the paper is organized as follows. In section 2 we outline salient characteristics of the numerical model and features of the land surface data assimilation system used to specify the initial surface conditions. A brief discussion of the design of simulations discussed in the paper is also provided. Section 3 presents an overview of simulation results and comparison with observations. The simulated convection initiation is analyzed in section 4, with land surface–atmosphere interaction mechanisms germane to the convection initiation discussed in section 5. A summary and concluding remarks are presented in section 6.

2. Numerical model and experiment design

a. Numerical model

The coupled fifth-generation Pennsylvania State University–National Center for Atmospheric Research nonhydrostatic Mesoscale Model (MM5)–land surface modeling system is the investigative tool used in this

study. MM5 (Grell et al. 1994) is configured for the current study with up to four two-way interactive grids having horizontal grid spacings of 30, 10, 3.3, and 1.1 km and grid point dimensions of 100 × 82, 142 × 124, 169 × 169, and 172 × 172, respectively. The locations of the nested domains, along with the terrain used in the 10-km (outermost) nest D2, are shown in Fig. 3. The coarse outer domain, D1, (not pictured) comprises the southwesternmost two-thirds of the continental United States and extends farther south into central Mexico, also covering the entire Gulf of California and much of the Gulf of Mexico.

MM5 is a terrain-following model that uses the sigma, $\sigma = (p - p_t)/(p_s - p_t)$, vertical coordinate, where p is the pressure, p_t is a specified top pressure, and p_s is the surface pressure. The same 31 half-sigma levels[1] were specified for all simulations. Pressure at the top of the model, where a radiative boundary condition is used, is 50 hPa. The lowest half-sigma level is located at 25–30 m AGL. Since a major objective of the current study is to examine the effect of surface–PBL interactions on deep convection initiation, vertical resolution is significantly enhanced in the lower troposphere.

The PBL scheme used in these simulations is based on that used in the National Centers for Environmental Prediction (NCEP) Eta operational Model, and is described by Janjic (1990, 1994). The parameterization predicts turbulent kinetic energy and allows local vertical mixing between individual layers within the PBL.

The Grell (1993) cumulus parameterization is used on both the outer domain and the 10-km nest for all simulations. Horizontal resolution is sufficient to resolve gross features of deep atmospheric convection on the 3.3- and 1.1-km nests, where no cumulus parameterization was used. An explicit microphysical scheme that predicts rain, snow, graupel, cloud water, and cloud ice is used on all domains. This scheme is based on Reisner et al. (1998) but has been modified to include graupel and ice number concentration prediction equations. A radiation scheme (Dudhia 1989), in which short- and longwave radiation interact with the ground, the clear atmosphere, clouds, and precipitation, is also used.

The LSM coupled to the MM5 (Chen and Dudhia 2001) is based on the Oregon State University (OSU) LSM (Pan and Mahrt 1987). Additions to the OSU version include an explicit vegetation canopy resistance formulation used by Jacquemin and Noilhan (1990) and the surface runoff scheme of Schaake et al. (1996). The LSM has a single canopy layer and predicts volumetric soil moisture and temperature in four soil layers. The depth of the individual soil layers from top to bottom are 0.1, 0.3, 0.6 and 1.0 m. The root zone is contained in the upper 1 m (top three layers).

[1] The half-sigma levels are located at σ = 0.996, 0.988, 0.979, 0.969, 0.958, 0.945, 0.930, 0.914, 0.895, 0.875, 0.852, 0.826, 0.797, 0.765, 0.730, 0.692, 0.650, 0.605, 0.556, 0.504, 0.449, 0.392, 0.333, 0.274, 0.215, 0.163, 0.121, 0.085, 0.055, 0.030, and 0.009.

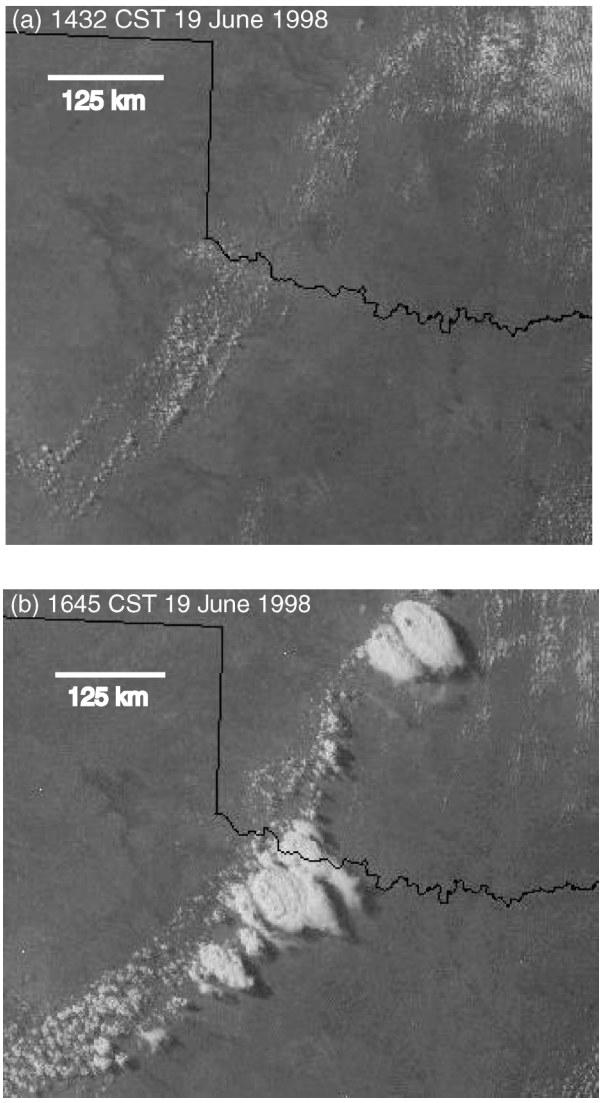

FIG. 1. *GOES-8* visible satellite imagery for (a) 1432 and (b) 1645 central standard time (CST) 19 Jun 1998. For UTC time add 6 h.

Communication between the LSM and the PBL occurs within the ''surface layer'' situated between the ground and the lowest half-sigma level of MM5. The MM5 surface layer parameterization provides heat and moisture exchange coefficients, which are passed to the LSM, together with the surface radiative forcing terms and precipitation rates. The LSM routine returns the surface heat and moisture fluxes to the PBL scheme for calculation of the boundary layer flux convergence, which contributes to the atmospheric temperature and moisture tendencies.

The exchange coefficients are obtained using Monin–Obukhov similarity theory, which requires vertical integrations between roughness lengths (heights) for momentum and heat, and the top of the surface layer (e.g., Chen and Dudhia 2001). Chen et al. (1997) discussed how appropriate roughness lengths for heat and moisture

(z_{0t}) may differ from that for momentum (z_{0m}), depending on surface characteristics and properties of the flow, and examined sensitivity of Eta Model fluxes obtained using both fixed ratios of z_{0m}/z_{0t} and ratios obtained using the Reynolds number–dependent formulation of Zilitinkevich (1995)

$$\frac{z_{0m}}{z_{0t}} = \exp(kC\mathrm{Re}^{*1/2}); \qquad \mathrm{Re}^* = \frac{u_0^* z_{0m}}{\nu}, \qquad (1)$$

where k is the von Kármán constant (0.4), ν is the kinematic molecular viscosity, Re* is the roughness Reynolds number, u_0^* is the surface friction velocity, and C is an empirical constant. Use of $C = 1.0$ in the current simulations resulted in realistic predictions of surface temperature, mixing ratio, and PBL depth.

b. Initialization

The initial and lateral boundary conditions for MM5 are supplied by analyses from the Rapid Update Cycle-2 (RUC-2) Regional Modeling and Data Assimilation System (Benjamin et al. 2004a,b). RUC-2 analyses, obtained on pressure levels spaced 25 hPa apart from 1000 to 100 hPa, are horizontally and vertically interpolated to all model grid points at the start of the simulation and to the lateral boundaries of D1 at subsequent 3-h intervals. Since the RUC-2 analyses terminate at 100 hPa, the 100-hPa-level data are extrapolated to the 50-hPa model top.

The high-resolution land data assimilation system (HRLDAS) described by Chen et al. (2004) was run prior to the simulations to obtain finescale (i.e., 4-km horizontal resolution) initial conditions of soil moisture/temperature, and vegetation variability for the LSM. HRLDAS makes use of multiple types of observed and analyzed conditions including, 1) National Weather Service (NWS) Office of Hydrology Stage-IV rainfall analyses performed on a 4-km national grid (Fulton et al. 1998); 2) 0.5° hourly downward solar radiation derived from *Geostationary Operational Environmental Satellites 8* and *9* (*GOES-8* and *GOES-9*), a product jointly developed by National Oceanic and Atmospheric Administration/National Environmental Satellite, Data, and Information Service (NOAA/NESDIS) and the University of Maryland (Pinker et al. 2002); 3) near-surface temperature, humidity, wind, downward longwave radiation, and surface pressure from 3-hourly NCEP Environmental Data Assimilation System (EDAS) analyses; 4) 1-km horizontal resolution United States Geological Survey (USGS) 24-category land use and 1-km horizontal resolution State Soil Geographic (STATSGO) soil texture maps; and 5) 0.15° monthly satellite-derived green vegetation fraction.

A comparison of the 0.1-m top layer 0600 central U.S. standard time (CST) 19 June 1998 EDAS soil moisture used to initialize the operational Eta Model (Fig. 4a) with that obtained from HRLDAS (Fig. 4b) shows much finer-scale structure from HRLDAS. Large regional differences between EDAS and HRLDAS, in both absolute soil moisture values and their mesoscale gradients, are also evident. Heavy rainfall, which occurred over the previous 12 h (Fig. 4c) near the south-central Oklahoma–north Texas border region (area A) and in eastern Oklahoma (area B), has a clear footprint in the HRLDAS soil moisture (Fig. 4b), contributing to wetter soil conditions in these regions than those found

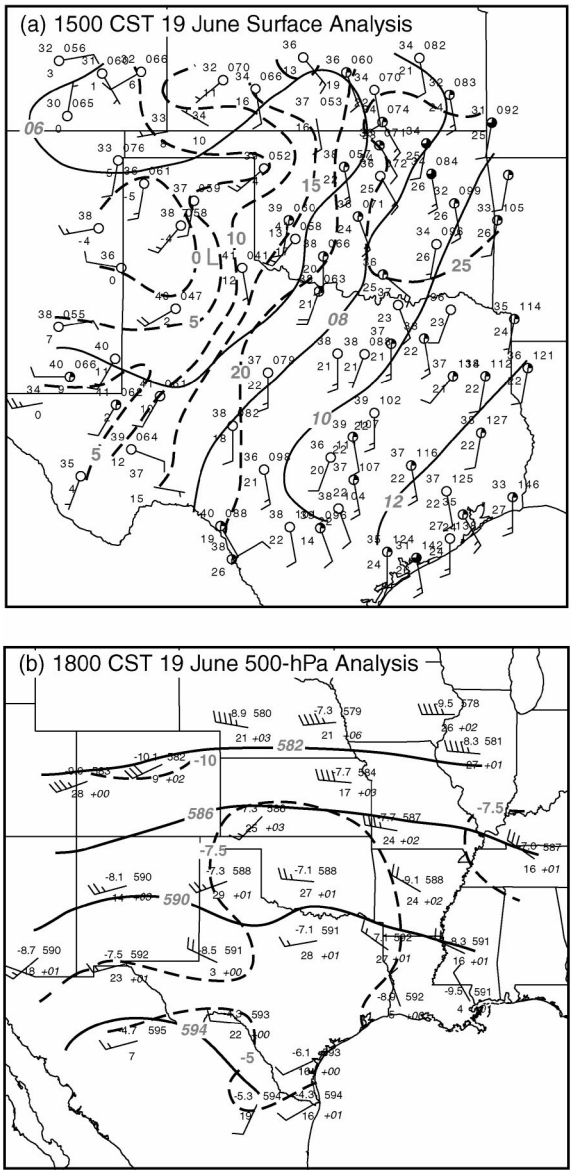

FIG. 2. (a) Surface map with pressure (solid lines) and dewpoint (dashed lines) subjectively analyzed in 2-hPa and 5°C intervals, respectively. Station model includes temperature (°C, upper left), dewpoint (°C, lower left), pressure (0.1 hPa with first digit omitted, upper right), cloud cover, and horizontal wind (kt). (b) 500-hPa map with geopotential height and temperature analyzed in 4-dam and 2.5°C intervals, respectively. Station model includes temperature (°C, upper left), dew point depression (°C, lower left), geopotential height (decameters, upper right), 12-h geopotential height tendency (dam, lower right), and horizontal wind (kt).

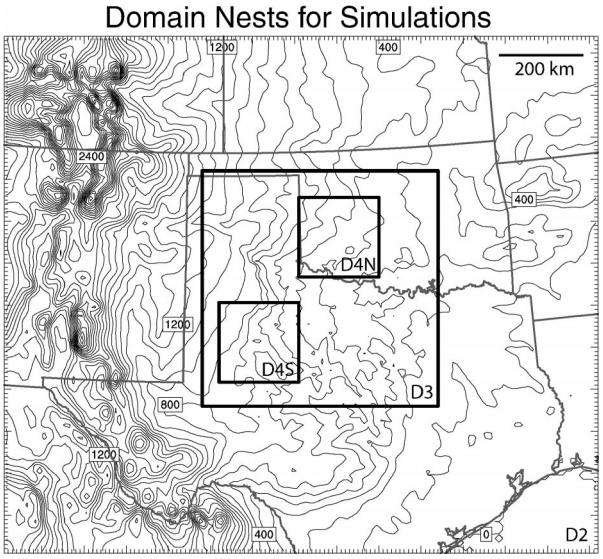

FIG. 3. Nested domains for various simulations elaborated in the text and later in Table 1. Terrain elevation for the first inner domain D2 is contoured in 100-m intervals.

in the EDAS analysis (Fig. 4a). Elsewhere, the EDAS analysis is typically wetter.

c. Simulations

The simulations discussed in this paper are designed to examine the daytime diurnal cycle of deep convection initiation in the SGP. Thus, we begin the simulations at 0600 CST (1200 UTC) 19 June 1998 and report results for up to 12 h of model integration. In all simulations discussed, the integration on the outer two domains begins at 0600 CST, with integration on the 3.3-km deep convection-resolving nest (D3 in Fig. 3) starting 1 h later at 0700 CST.

The primary simulation that we discuss (HRESM3) utilizes the finescale initial land surface conditions (including soil moisture) obtained from HRLDAS. Two closely related simulations, HRESM4S and HRESM4N, with additional 1.1-km nests (D4S and D4N, respectively, in Fig. 3), were integrated starting in late morning at 1100 CST ($t = 5$ h) with D3 from HRESM3 providing initial and boundary conditions for the 1.1-km nests. The purpose of these two individual higher-resolution simulations is to investigate finescale aspects of convection initiation in different locations along the southwest–northeast (SW–NE)-oriented surface q_v gradient zone (e.g., Fig. 2a). We emphasize, however, that the general character of convection initiation is adequately represented on the areally extensive 3.3-km domain. Since we have an interest in examining the interaction of multiple scales of motion, up to those of large mesoscale circulations (i.e., $L \geq 100$ km), the majority of our analysis of model output is performed on D3 of HRESM3.

A major objective of the current study is to determine the sensitivity of convection initiation to finescale representation of the soil moisture conditions for an observed case. Thus, we compare results of HRESM3 with an identically configured and executed simulation (ETASM3) that utilizes the much coarser initial specification of soil moisture from EDAS (Fig. 4a), instead of that from HRLDAS (Fig. 4b) used in HRESM3. A listing of all simulations discussed in this paper and their salient features is provided in Table 1.

3. Overview of simulations and comparison with observations

A mesoscale surface q_v gradient stretches southwestward from north-central Oklahoma into southwest Texas (Fig. 5a) at 0700 CST on D3 in the control simulation (HRESM3). By early to midafternoon the simulated q_v gradient has evolved into an intense dryline across west Texas with a maximum horizontal gradient of ~ 1 g kg^{-1} km^{-1} over about 15 km (Fig. 5b). Although the q_v gradient intensifies during the afternoon over the Texas–southwest Oklahoma border region into north-central Oklahoma, it fails to reach the intensity of the west Texas dryline prior to the local development of deep convection. Differences in motion are also evident as the Oklahoma q_v gradient remains quasi-stationary while the west Texas dryline moves eastward during the afternoon.

a. Simulated and observed rainfall

Heavy convective rainfall initiates in HRESM3 both along and up to 50 km east of the leading edge of the q_v gradient by mid-to-late afternoon (Fig. 6a). Convection first initiates directly along the strongest portion of the dryline in west Texas at 1500 CST, while subsequent convection develops ~ 1 h later from southwest to northeast near the weaker q_v gradient that extends from the southwest Oklahoma–Texas border region into north-central Oklahoma.

The simulated convective rainfall and its relationship to the dryline position depends on the soil moisture initialization. Despite strong similarities to HRESM3 over Oklahoma, in ETASM3, which uses coarser and generally wetter initial soil moisture conditions, the majority of the convection over Texas develops ~ 130 km east of the dryline (Fig. 6b), whereas convection initiation occurs either directly along or much closer to the dryline, in both HRESM3 (Fig. 6a) and the observations (Figs. 2 and 6c). Only a few isolated storms occur along or adjacent to the dryline in ETASM3, despite an even stronger dryline q_v gradient in ETASM3 than in HRESM3 (cf. Figs. 6a,b).

The rainfall intensity and areal coverage is greater along the simulated dryline in HRESM3 (Fig. 6a) than in the observations (Fig. 6c). However, the timing of convection initiation and the ~ 100-km width of the sim-

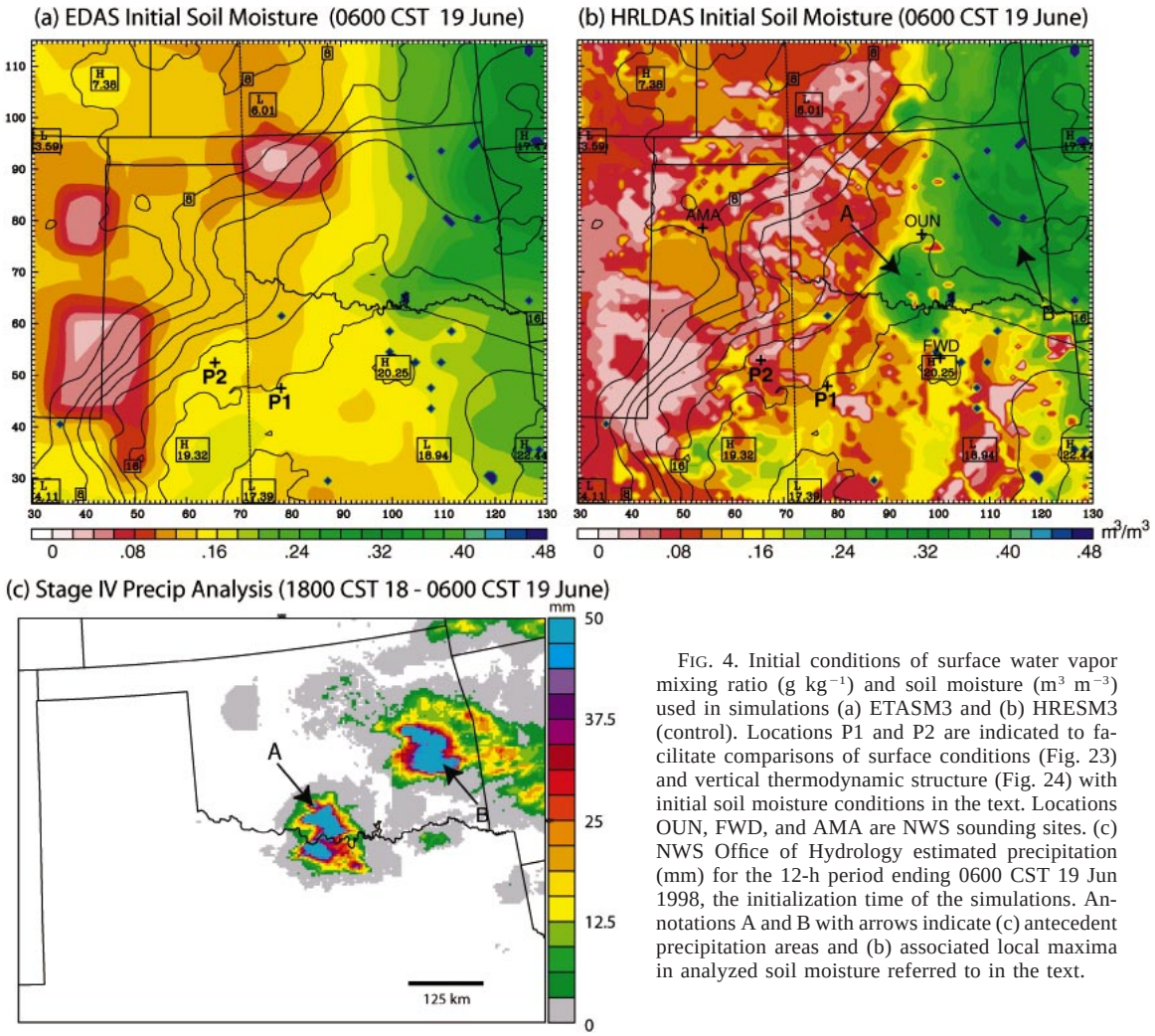

FIG. 4. Initial conditions of surface water vapor mixing ratio (g kg^{-1}) and soil moisture (m^3 m^{-3}) used in simulations (a) ETASM3 and (b) HRESM3 (control). Locations P1 and P2 are indicated to facilitate comparisons of surface conditions (Fig. 23) and vertical thermodynamic structure (Fig. 24) with initial soil moisture conditions in the text. Locations OUN, FWD, and AMA are NWS sounding sites. (c) NWS Office of Hydrology estimated precipitation (mm) for the 12-h period ending 0600 CST 19 Jun 1998, the initialization time of the simulations. Annotations A and B with arrows indicate (c) antecedent precipitation areas and (b) associated local maxima in analyzed soil moisture referred to in the text.

ulated NE–SW-oriented heavy rainfall zone near the dryline in HRESM3 is similar to observations. In the remainder of the paper we focus on the interaction between surface and multiscale atmospheric processes and their relationship to these aspects of the convection initiation.

b. Simulated and observed surface evolution

The accuracy of the simulated surface conditions is more difficult to verify than the simulated rainfall due to the relatively coarse resolution of the surface observations. However, the available observations compare favorably with collocated model (HRESM3) output, which suggests that the model is handling important physical processes such as the sensible and latent heat fluxes, horizontal advections, and vertical mixing in a reasonable fashion.

Following Shaw et al. (1997), we compare hourly surface observations of temperature and moisture variables with corresponding values from the lowest model level (25–30 m AGL) grid points of HRESM3 (Fig. 7). The locations are those of the NWS stations (Fig. 5b) closest to the afternoon q_v gradient on both sides. Although observations are generally 1°–2°C warmer from midmorning (1000 CST) onward, the observations and simulation undergo similar evolutions. We speculate that the cooler simulated conditions may arise, in part, from shallow surface-based superadiabatic layers not being fully captured in the simulation.

TABLE 1. Domains and initial soil conditions used in simulations. Horizontal grid spacing of innermost domain in parentheses. Control simulation in boldface.

Name	Domains	Initial soil condition
HRESM4S	D1, D2, D3, D4S (1.1 km)	HRLDAS
HRESM4N	D1, D2, D3, D4N (1.1 km)	HRLDAS
HRESM3	**D1, D2, D3 (3.3 km)**	**HRLDAS**
ETASM3	D1, D2, D3 (3.3 km)	EDAS
HRESM2	D1, D2 (10 km)	HRLDAS

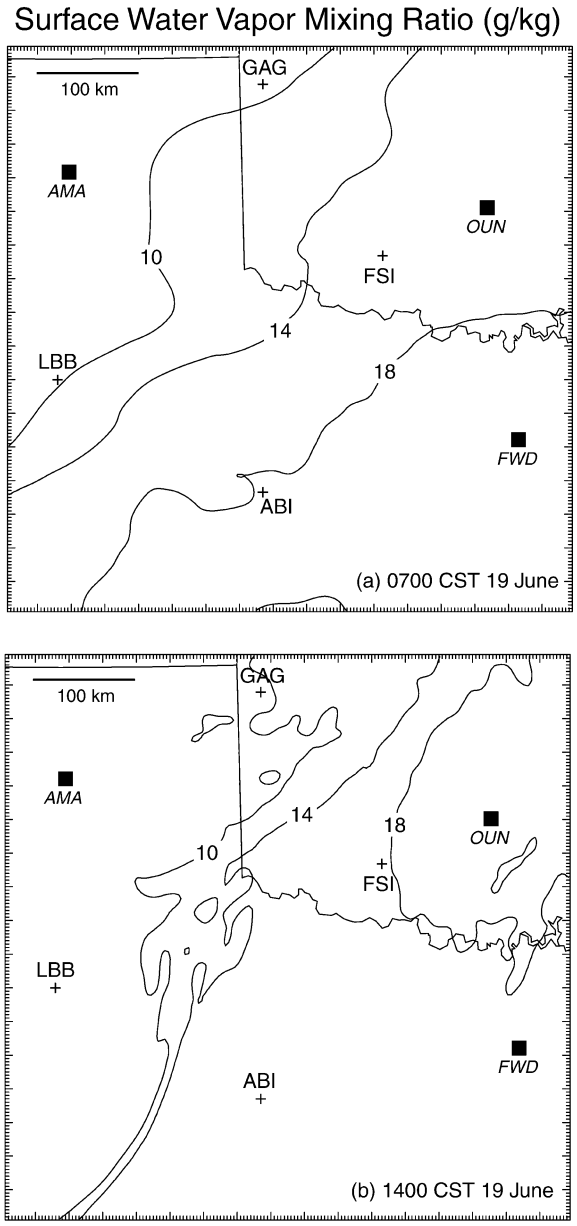

FIG. 5. Simulated surface water vapor mixing ratio (g kg^{-1}) at (a) 0700 CST (initialization time for domain 3), and (b) 1400 CST 19 Jun 1998. Annotations indicate NWS surface (crosses) and sounding (darkened squares) station locations referred to in the text and subsequent figures.

Along the east side of the q_v gradient, surface temperatures increase steadily in both Texas (ABI; Fig. 7a) and southwestern Oklahoma (FSI; Fig. 7c) through early to midafternoon (1400 CST). Surface dewpoints are decreasing slightly at both stations by early afternoon as PBL growth promotes vertical mixing of drier air from aloft (Figs. 8a,b). Contrasts in surface evolution among stations on the west side of the afternoon q_v gradient are more significant than on the east side. At Lubbock, Texas (LBB), a decrease in dewpoint (most rapid in the observations) begins only a few hours after sunrise (Fig. 7b), whereas farther north at Gage, Oklahoma (GAG), the dewpoint in both the model and observations increases significantly in the morning and does not begin decreasing until midday (Fig. 7d). This regional difference can be attributed to several factors including stronger horizontal moisture advection and latent heat fluxes (Fig. 9a), and greater moisture content immediately above the shallow 0800 CST PBL at GAG (Fig. 10c) than at LBB (Fig. 10a).

The surface q_v gradient intensifies over west Texas during the morning as local q_v decreases accompanying the rapid PBL growth on the west side of the gradient [e.g., near LBB (Fig. 10a)], are greater than on its east side [e.g., near ABI (Fig. 8a)]. By late morning, surface confluence is evident within the q_v gradient zone between LBB and ABI resulting from the development of an enhanced westerly wind component on the west side (Fig. 9a), which intensifies further by midafternoon (Fig. 9b). It is during this period from late morning into midafternoon that the southern portion of the Texas q_v gradient intensifies into a strong dryline with moisture contrasts approaching 1 g kg^{-1} km^{-1} (Fig. 9b).

Previous modeling and observational studies (e.g., Schaefer 1974; McCarthy and Koch 1982; Sun and Wu 1992; Hane et al. 1997) have attributed similar intensification of westerlies on the west side of the surface q_v gradient and the initial intensification and eastward motion of the q_v gradient to the turbulent vertical mixing of dry air with stronger westerly momentum down to the surface. Evolution of the simulated zonal wind component west of the dryline at LBB (Fig. 10b) is consistent with vertical mixing during rapid PBL growth between 1100 and 1700 CST (Fig. 10a). The afternoon changes in the simulated zonal wind profile at GAG (Fig. 10d) on the dry side of the much weaker Oklahoma portion of the surface q_v gradient are also consistent with vertical momentum transport. However, here, the surface westerlies are weaker and slower to develop, consistent with less rapid PBL growth (Fig. 10c).

The establishment of surface confluence on the west side of the q_v gradient in Texas coincides with the evolution of this portion of the gradient into a strong dryline (Fig. 9b). Recent studies (e.g., Grasso 2000) have indicated that dryline development can occur in two distinct phases, the first being associated with the lateral differences in eddy vertical mixing of wind and moisture discussed earlier, with subsequent intensification of the horizontal moisture gradient arising from adiabatic frontogenetical process.

To examine the role of the resolved-scale flow on dryline intensification in the current case we analyze the two-dimensional adiabatic form of the frontogenesis equation for water vapor:

$$\frac{D}{Dt}\left(\frac{\partial q_v}{\partial x}\right) = -\frac{\partial u}{\partial x}\frac{\partial q_v}{\partial x} - \frac{\partial v}{\partial x}\frac{\partial q_v}{\partial y} - \frac{\partial w}{\partial x}\frac{\partial q_v}{\partial z}, \qquad (2)$$

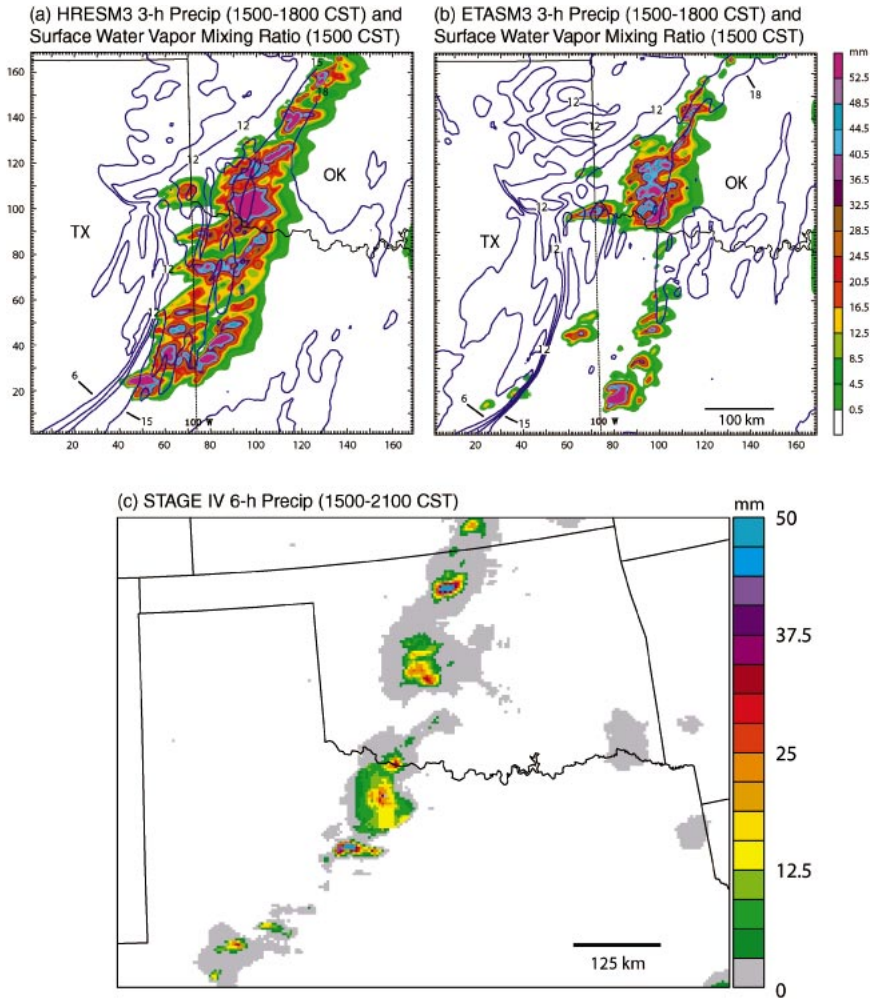

FIG. 6. Simulated 3-h precipitation from 1500 to 1800 CST 19 Jun 1998 (t = 9–12 h) in color scheme with 4-mm intervals starting at 0.5 mm and 1500 CST 19 Jun (t = 9 h) surface water vapor mixing ratio in blue contours with 3 g kg^{-1} intervals starting at 6 g kg^{-1} for domain 3 of simulations (a) HRESM3 and (b) ETASM3. (c) As in Fig. 4c but for the 6-h period ending 2100 CST 19 Jun 1998.

where the x coordinate is oriented along line AB of Fig. 9b, which is approximately parallel to the surface horizontal moisture gradient. The terms on the right-hand side of (2) represent forcing of the q_v gradient due to confluence, shear, and tilting, respectively.

We examine terms on the right side of (2) within a vertical cross section that is averaged for 100 km in the y direction (i.e., normal to line AB). The shear term represents the turning or reorientation, by the horizontal shear, of the portion of the moisture gradient normal to the cross section into the plane of the cross section. This term is more than an order of magnitude weaker than the confluence and tilting terms, owing to the approximate two-dimensionality of the moisture gradient (Fig. 9b) and the fact that we have oriented the coordinate system such that the moisture gradient is negligible in the direction normal to AB. Figure 11 presents the remaining two forcing terms—confluence and tilting. As found by Grasso (2000), the simulated surface water vapor frontogenesis is dominated by confluence of the horizontal wind (Fig. 11a). Localized variations in PBL depth, which result from differential vertical motion associated with turbulent roll-like circulations, contribute to large magnitudes of the tilting term that extend from the top of the PBL into the inversion layer above (Fig. 11b). The influence of these roll-like circulations on convection initiation is discussed in section 4.

The Oklahoma surface mesonet (Brock et al. 1995), which has a mean station spacing of about 30–40 km, permits a more detailed verification of the simulated surface structural characteristics in the vicinity of the weaker northern portion of the q_v gradient. The early afternoon (1300 CST) q_v gradient zone that extends from southwestern into north-central Oklahoma is relatively broad (~100–150 km) and lacks an abrupt wind shift with strong convergence in both HRESM3

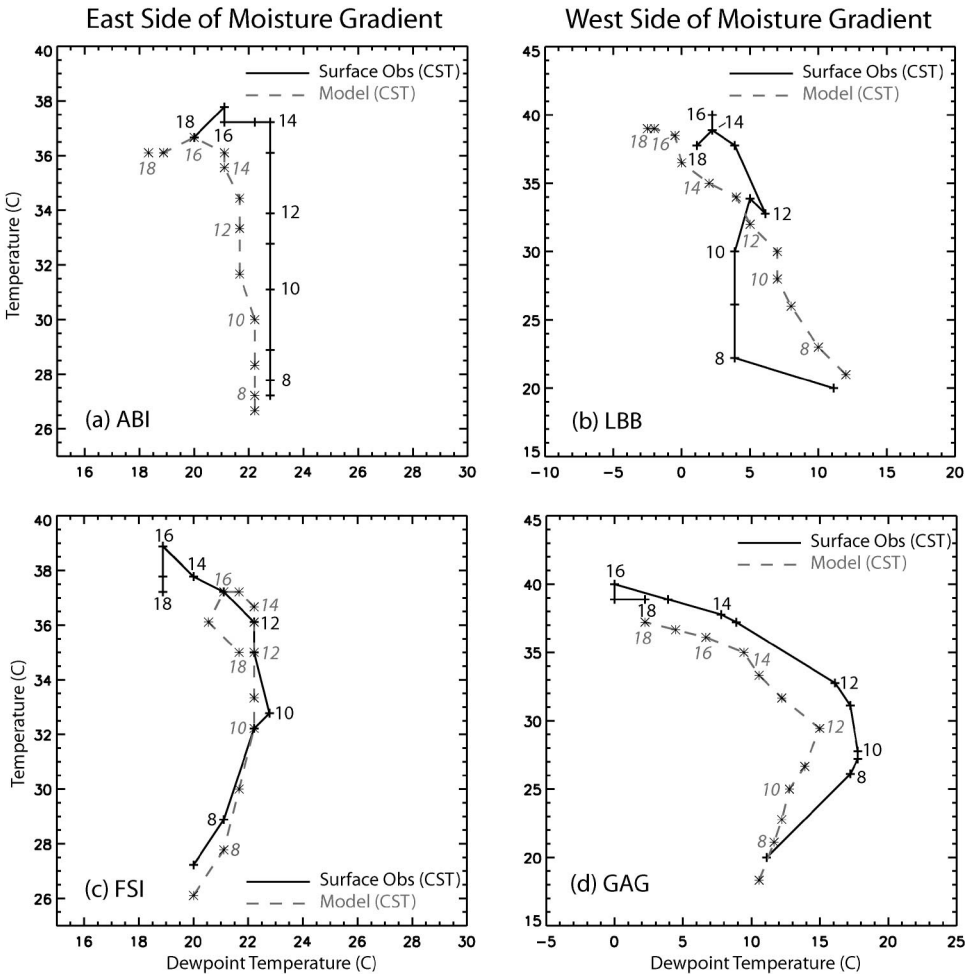

FIG. 7. Comparison of observed temperature and dewpoint data (solid) at NWS reporting stations of (a) Abilene, TX (ABI), (b) Lubbock, TX (LBB), (c) Fort Sill, OK (FSI), and (d) Gage, OK (GAG) 19 Jun 1998 with corresponding (horizontally collocated) values obtained at the lowest vertical grid points on domain 3 of simulation HRESM3.

(Fig. 12a) and the mesonet data (Fig. 12b). Locally enhanced θ_v in the vicinity of the q_v gradient from midmorning through early afternoon is a common feature of the simulations and the observations (Fig. 12). Both the origin of the zone of enhanced θ_v and its close relationship to convection initiation (Fig. 6) are discussed in sections 4 and 5.

c. Simulated and observed vertical structure

The vertical thermodynamic structure in the dryline environment is crucial in determining the timing and location of convection initiation. Unfortunately the location of the twice-daily NWS radiosondes did not coincide with the q_v gradient region. However, 1800 CST soundings were launched both east, at Norman, Oklahoma (OUN), and Dallas/Fort Worth, Texas (FWD), and west of the late afternoon q_v gradient at Amarillo, Texas (AMA). Soundings from these locations (Fig. 5) are compared to collocated model soundings in Fig. 13. East of the q_v gradient, both the observations and HRESM3 exhibited a shallow ~100-hPa-deep PBL with $\overline{q}_v \sim 18$ g kg^{-1} near the western edge of the large soil moisture region (Fig. 4b) at OUN (Fig. 13a). Over drier soils at Dallas/Fort Worth (FWD) east of the Texas dryline (Fig. 13b) and Amarillo (AMA) west of the Texas dryline (Fig. 13c), the simulated PBL is slightly (~1 g kg^{-1}) moister than observed.

The late afternoon PBL west of the dryline is too dry to support deep convection (Fig. 13c). In contrast, abundant conditional instability results from the moist PBL at both OUN (Fig. 13a) and FWD (Fig. 13b). However, 50–100-hPa-deep stable layers of moderate strength surmount the PBL and are able to inhibit deep convection in the absence of strong forcing at these locations 100–200 km east of the q_v gradient in both the observations and HRESM3.

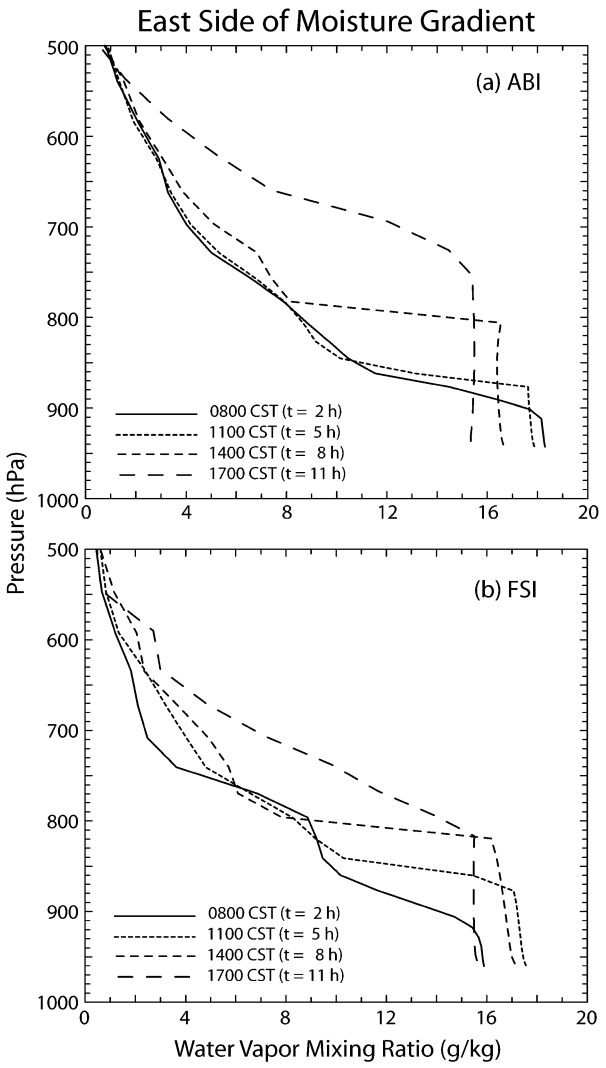

FIG. 8. Evolution of the vertical structure of water vapor mixing ratio, q_v, 19 Jun 1998 for domain 3 of simulation HRESM3 at horizontal grid locations corresponding to the NWS surface stations of (a) Abilene, TX (ABI) and (b) Fort Sill, OK (FSI). Station locations are indicated in Fig. 5.

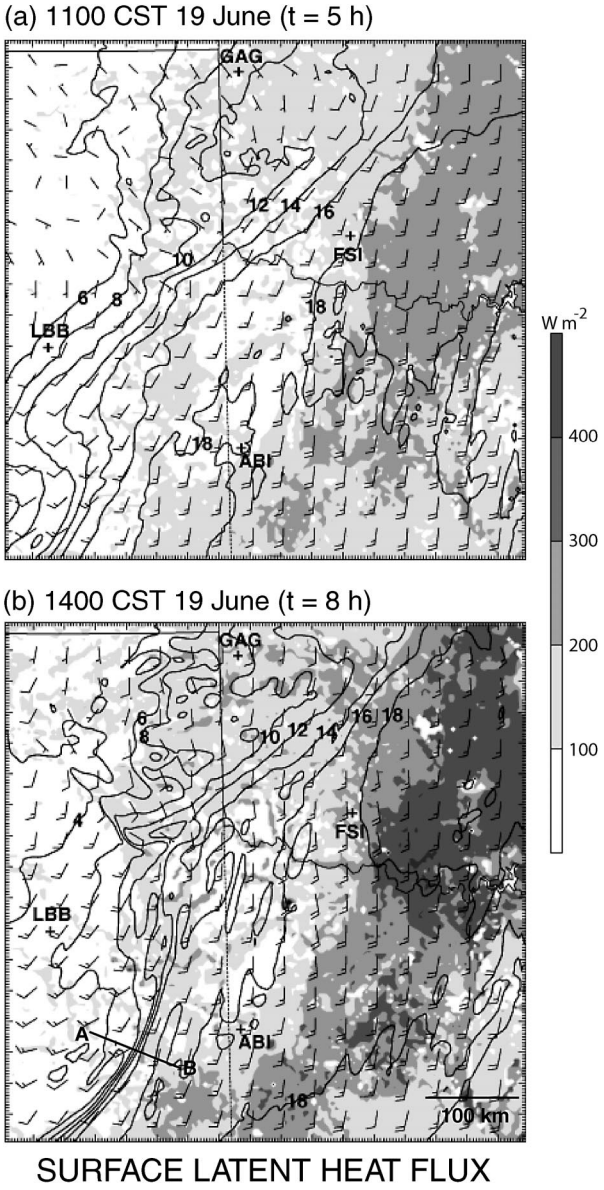

FIG. 9. Horizontal winds and water vapor mixing ratio, q_v (2 g kg^{-1} contour interval) at the lowest model vertical grid point, and surface latent heat flux (100 W m^{-2} shading intervals) for domain 3 of simulation HRESM3 at (a) 1100 and (b) 1400 CST 19 Jun 1998. Annotated locations refer to the NWS surface station sites. (b) Line AB denotes the location of the line-averaged vertical cross section displayed in Fig. 11.

4. Convection initiation

Despite significant differences in intensification of the surface q_v gradient zone from west Texas to north-central Oklahoma, simulated deep convection developed along nearly its entire SW–NE extent in HRESM3 (Fig. 6a). This suggests that processes other than those occurring directly at the intense portion of the q_v gradient play an important role in convection initiation.

The simulated convective precipitation in both HRESM3 and ETASM3 generally occurs along and east of the q_v gradient in locations where the afternoon PBL depth (Fig. 14) is greatest. The PBL vertical velocity patterns near the time convection initiation (Fig. 15) indicate a strong localized updraft along a NW–SE-oriented confluence zone in the Texas Panhandle, where conditions were too dry (q_v = 4–8 g kg^{-1}) to support deep convection. Also evident is a broader mesoscale zone that contains PBL updrafts and downdrafts elongated in the direction of the horizontal wind both east and west of the q_v gradient. At 1500 CST (Fig. 15), these vertical motions are most intense within the deep PBL near the Texas dryline, but also occur within the local maximum of PBL depth on the east side of the weaker q_v gradient in Oklahoma (cf. Fig. 14).

The simulated deep convection during the next hour

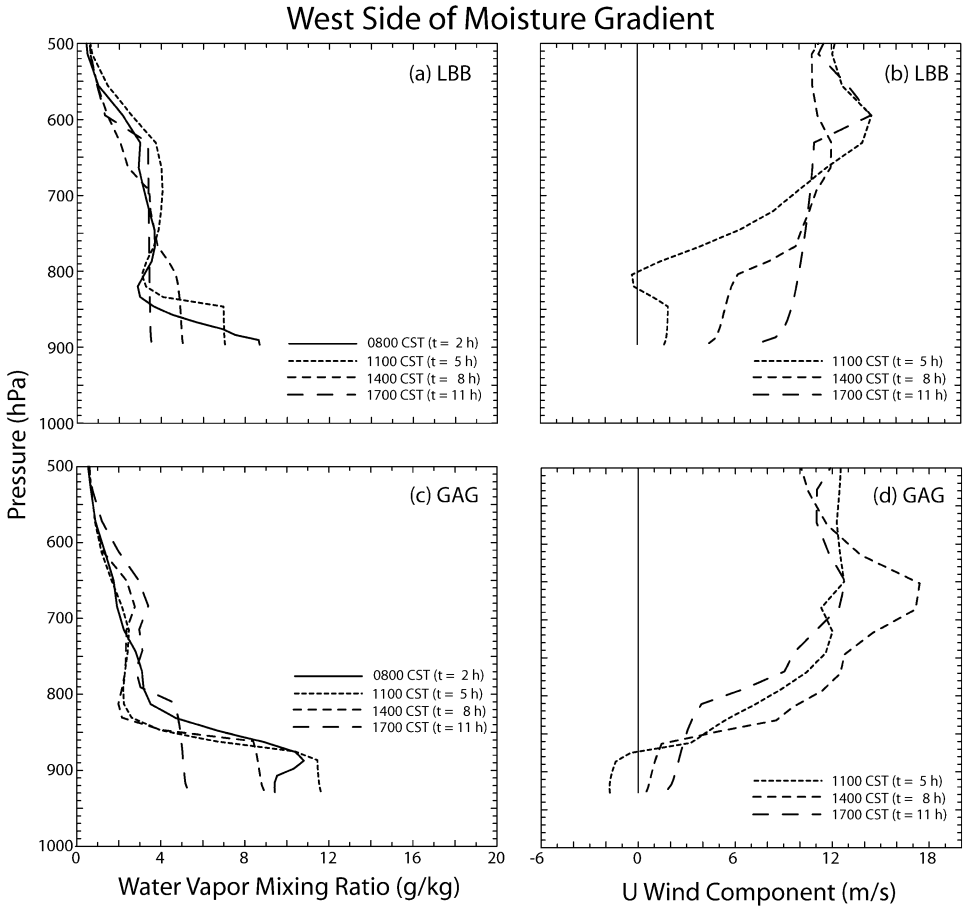

FIG. 10. As in Fig. 8 but for the model locations corresponding to (a) Lubbock, TX (LBB) and (c) Gage, OK (GAG), and with the vertical structure of the zonal component of the horizontal wind instead of water vapor mixing ratio at (b) LBB and (d) GAG.

occurs along and immediately northeast (i.e., downwind relative to the midtropospheric flow) of the most intense elongated PBL updrafts located along and slightly east of the dryline (Fig. 15). The simulated deep convection initiation over Texas in HRESM3 (Fig. 15a) is similar both in location and character to the development of deep convection from within preexisting cumulus cloud streets that may be inferred from visible satellite observations (Fig. 1). Simulated deep convection also initiates from the elongated updrafts on the east side of the q_v gradient in Oklahoma (Fig. 15); however, it lags the simulated convection initiation near the Texas dryline by 1 to 1.5 h (not shown).

Previous observational (Atkins et al. 1998) and numerical (Ziegler et al. 1997) studies have noted similar elongated vertical velocity features along the mean PBL wind that are associated with convection initiation. These authors have suggested that such vertical motions may be a manifestation of horizontal convective rolls (HCRs) generated by intense surface heating. In the current case, the strongest vertical motions (Fig. 15) are located where the PBL depth (Fig. 14) is greatest. This is not surprising since the turbulent convective plumes generated by surface sensible heat flux are a major factor in deepening the PBL. However, the relatively weak maximum vertical velocities of 0.5 to 1 m s^{-1} at 1500 CST and large aspect ratios of $L/D = 15$–25, where D is the PBL depth and L is the horizontal spacing between adjacent PBL updraft maxima, suggest that these circulations are underresolved on the 3.3-km horizontal grid.

Two other simulations, one employing an additional $\Delta x, y = 1.1$-km nest centered along a limited portion of the Texas dryline (HRESM4S, location shown in Fig. 15a) and the other encompassing the weaker q_v gradient in Oklahoma (HRESM4N, location shown in Fig. 15a) also exhibit HCRs, but appear to have more random PBL vertical velocity structure at greater distances from the southern inflow boundary (Figs. 16a,b). Although detailed observations are not available for comparison, the simulations with the additional higher-resolution nest appear to more realistically resolve these finescale PBL circulations. For example, the aspect ratios of $L/D = 6$–12 of the HCRs on the finest grids of HRESM4S

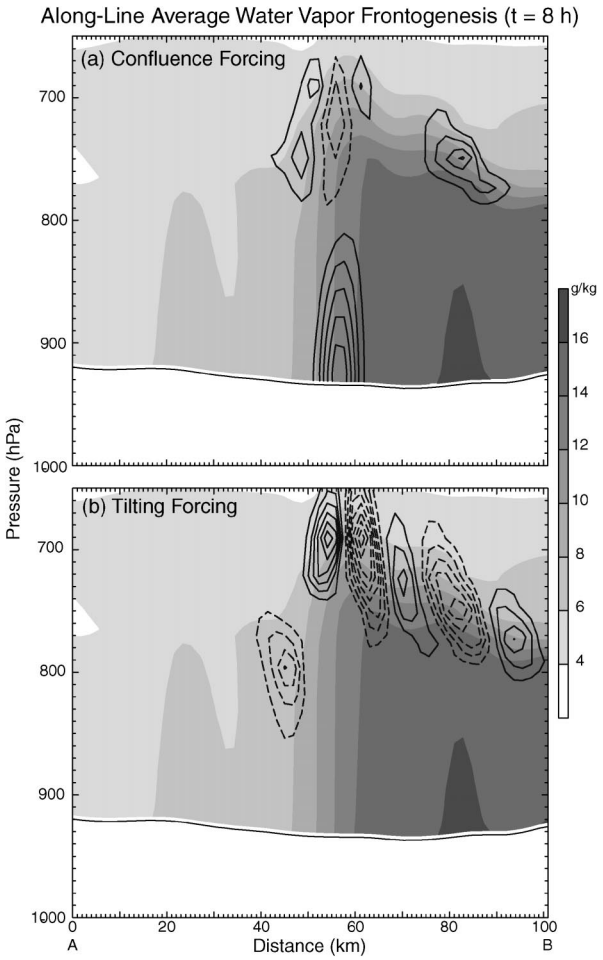

FIG. 11. Vertical cross section of simulated frontogenetic forcing of water vapor mixing ratio [contour interval of 2 g (kg km h)$^{-1}$, zero contour omitted] due to (a) confluence and (b) tilting effects at $t = 8$ h (1400 CST 19 Jun 1998) along line AB of D3 of simulation HRESM3 in Fig. 9b that is horizontally averaged over a 100-km distance (centered on AB) in the direction perpendicular to the cross section. Shading represents the $t = 8$ h line-averaged values of water vapor mixing ratio in intervals of 2 g kg^{-1}.

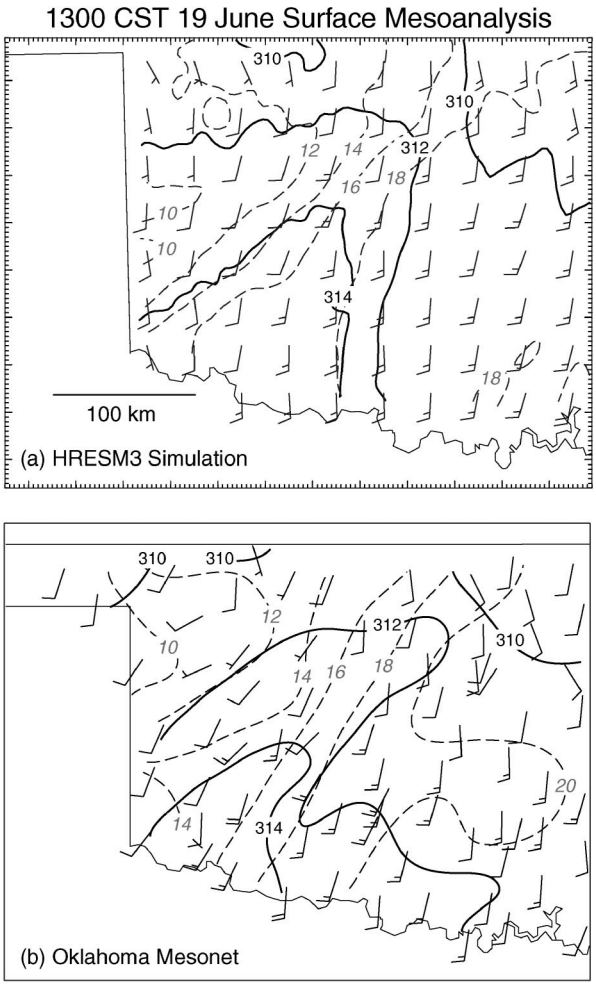

FIG. 12. 1300 CST 19 Jun 1998 ($t = 7$ h) horizontal winds and mesoanalysis of virtual potential temperature, θ_v (solid) and water vapor mixing ratio (dashed) for (a) the lowest model level (25–30 m AGL) on a portion of domain 3 of simulation HRESM3 and for (b) a similar domain consisting of observations from the Oklahoma surface Mesonet. (a) The simulated data were analyzed using the MM5 graphics package RIP, whereas (b) the mesonet data analyzed were subjectively contoured.

and HRESM4N are significantly smaller than those on the 3.3-km horizontal grid of HRESM3 and are, accordingly, more consistent with observations of PBL roll vortices (e.g., LeMone 1973; Etling and Brown 1993). However, the fact that the deep convection in the 1.1-km simulations begins 1 to 2 h earlier than in either HRESM3 or the observations suggests that the strength of the simulated PBL turbulence on the finest grids could be somewhat too intense.

As is the case on the 3.3-km domain, deep convection initiates at the sites of the strongest PBL updrafts. Vertical cross sections taken across HCR circulations at the both the Texas dryline (Fig. 16a) at the east edge of the weaker Oklahoma q_v gradient (Fig. 16b) about 10 min prior to convection initiation show developing clouds situated above intense 3–5 m s^{-1} PBL updrafts (Figs. 16c,d). PBL water vapor mixing ratios are locally enhanced (diminished) within the updrafts (downdrafts) by up to several g kg^{-1}, as found in observations of HCRs (e.g., Weckwerth et al. 1996). Convective available potential energy (CAPE) and CIN, calculated at each model grid point using θ_v (e.g., Doswell and Rasmussen 1994), are displayed within the Texas and Oklahoma cross sections in Figs. 16e and 16f, respectively. Both moister and warmer (not shown) conditions within PBL updrafts resulted in locally enhanced CAPE and CIN being either zero or negligible (i.e., CIN $\leq w_{\max}^2/2$ m^2 s^{-2}) for air parcels that originate at any level within the PBL prior to the initiation of deep convection above.

Statistics of the 1400 CST vertical velocity at the horizontally varying PBL top were computed for simulations HRESM4N, HRESM3, and HRESM2 within

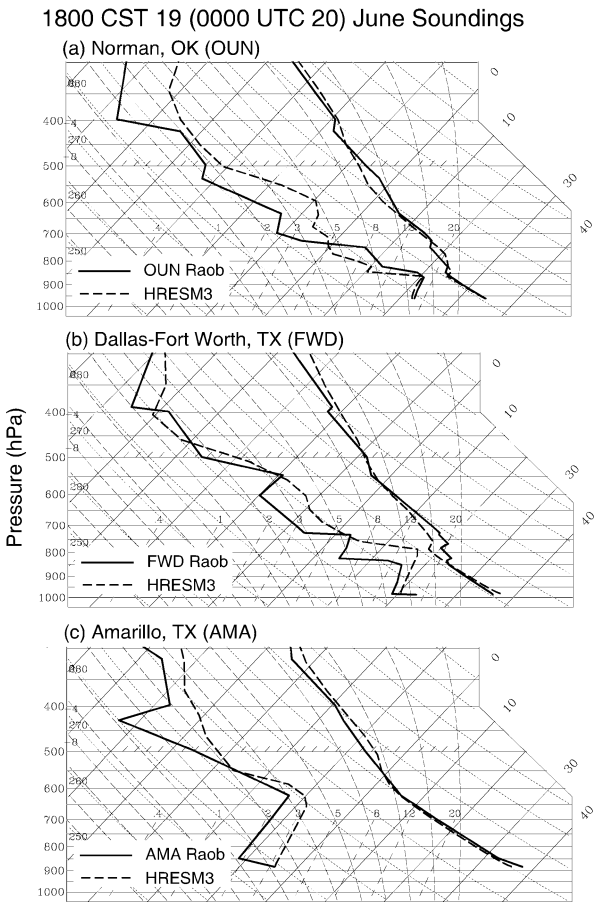

FIG. 13. Here, 1800 CST 19 Jun 1998 (t = 12 h) skew$T$–log$p$ profiles of temperature and moisture obtained at NWS sounding sites (solid curves) and from the horizontal grid points in simulation HRESM3 (dashed curves) closest to (a) Norman, OK (OUN), (b) Dallas/Fort Worth, TX (FWD), and (c) Amarillo, TX (AMA). The NWS sounding locations are depicted in Fig. 5.

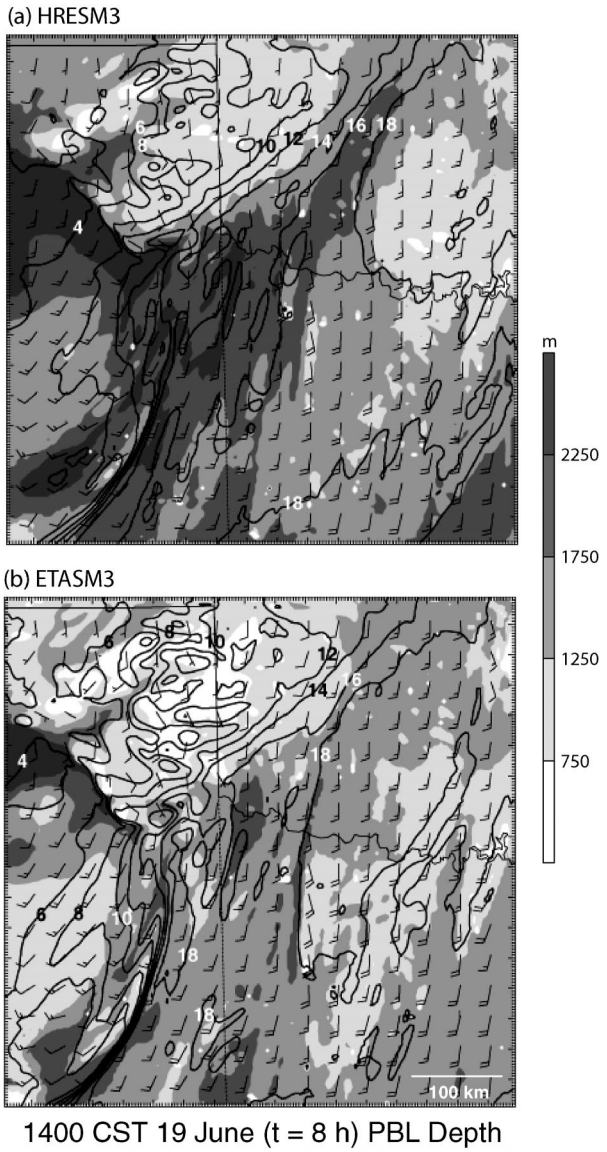

FIG. 14. Horizontal winds and water vapor mixing ratio, q_v (2 g kg^{-1} contour interval) at the lowest model vertical grid point, and planetary boundary layer (PBL) depth (500-m shading intervals) for domain 3 of simulations (a) HRESM3 and (b) ETASM3 at 1400 CST 19 Jun 1998 (t = 8 h).

the Oklahoma convection initiation zone approximated by the area bounded by the 375- and 525-m terrain contours in Fig. 16b. Each simulation exhibits mean PBL top ascent of $\overline{w}$ = 2–3 cm s^{-1} (Fig. 17) within this mesoscale zone. When $\overline{w}$ is removed, the resulting vertical velocity w' is negative (positive) over 57% (43%) of the convection initiation area in the 1.1-km simulation HRESM4N (Fig. 17a). The w' frequency distribution of HRESM4N (Fig. 17a) further indicates $w' > 0$ dominating $w' < 0$ for $|w'| > 0.81$ cm s^{-1}, whereas $w' < 0$ dominates $w' > 0$ at weaker magnitudes. Weaker and more areally extensive downdrafts adjacent to narrow intense updrafts is a well known characteristic of organized PBL turbulence (e.g., Stull 1988). Although less pronounced than for w', this bias is also evident for the total vertical velocity $w = \overline{w} + w'$ in HRESM4N (not shown).

In the 3.3-km simulation (HRESM3), the bias toward a greater number of weaker downdrafts is evident only after the mean ascent is removed, with $w' < 0$ ($w' > 0$) over 53% (47%) of the Oklahoma convection initiation area (Fig. 17b). Here, the strongest 1400 CST PBL updrafts are a full order of magnitude weaker (0.3 m s^{-1} versus 4.6 m s^{-1}) than in HRESM4N, and are not able to initiate deep convection until after they have intensified to ~1 m s^{-1} about 1.5 h later (not shown). The w' frequency distribution in the still coarser 10-km simulation (HRESM2), where cumulus parameterization is required to initiate deep convection, is nearly symmetric about zero (Fig. 17c), which is consistent with the lack of resolved turbulent motions.

In summary, we find that the simulated deep convection in both Texas and Oklahoma first initiates where

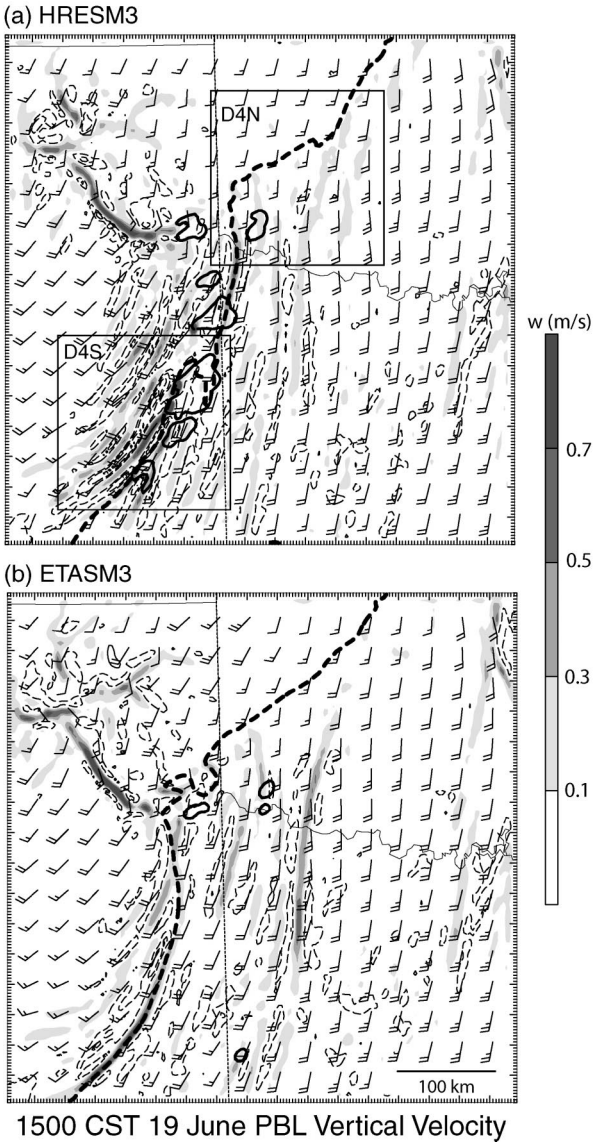

FIG. 15. Domain 3 1500 CST 19 Jun 1998 ($t = 9$ h) PBL horizontal wind and vertical velocity (values ≥ 10 cm s^{-1} shaded in 20 cm s^{-1} intervals and values ≤ -10 cm s^{-1} contoured with thin dashed lines in intervals of -20 cm s^{-1}) for the $\sigma = 0.895$ level of simulations (a) HRESM3 and (b) ETASM3. The bold solid contours represent 1-h simulated rainfall exceeding 4 mm from 1500 to 1600 CST 19 Jun 1998 ($t = 9$–10 h), and the bold dashed line is the $\sigma = 0.996$ (lowest model grid point) water vapor mixing ratio contour of 14 g kg^{-1}, which symbolically represents the approximate center of the initial surface moisture gradient (Fig. 5a). (a) The solid rectangles with annotations D4S and D4N, represent the locations of domain 4 of simulations HRESM4S and HRESM4N presented in Figs. 15a and 15b, respectively.

the PBL is locally deepest. Strong PBL updrafts of order 1 m s^{-1} are necessary to initiate deep convection, and deep convection occurs only in areas of localized PBL q_v maxima where absolute values are sufficient to support moderate-to-large CAPE with negligible CIN. These findings agree with those of Ziegler et al. (1997) and Ziegler and Rasmussen (1998) from previous observations and simulations of multiple dryline cases during the Cooperative Oklahoma Profiler Studies (COPS-91). In addition to the simulated finescale turbulent vertical motions, mean ascent of several cm s^{-1} occurs over the convection initiation region in Oklahoma. The occurrence of mean ascent of similar intensity in simulation HRESM2, which is unable to resolve finescale PBL circulations, suggests that the mean ascent in the convection initiation region may have a substantial mesoscale component. Although small-scale PBL circulations are directly responsible for convection initiation on the finer grids, mesoscale ascent can provide a more favorable environment for convection initiation. In the next section we demonstrate how land surface–atmosphere interactions result in differential sensible heating and a mesoscale vertical circulation, which act together to focus the mesoscale region of enhanced PBL depth and thermodynamic instability.

5. Influence of land surface–atmosphere interactions

a. Differential surface sensible heating

The simulated early afternoon PBL depth at 1400 CST ($t = 8$ h) is spatially correlated, over most of D3, with the time-averaged sensible heating from the previous 4 h (Fig. 18a). Thus it is of interest to understand the factors that govern the distribution and intensity of the sensible heating. The model sensible heating is given by $S = C_H U(T_g - T_{\text{sfc}})$, where U is the wind speed at the lowest model level (25–30 m), T_g is the ground (skin) temperature, T_{sfc} is the air temperature at the top of the surface layer, and C_H is the surface heat exchange coefficient.

The term $T_g - T_{\text{sfc}}$ (Fig. 18b) is generally largest over the western part of D3 in HRESM3, where the soil is dry (cf. Fig. 4b). However, the position of the time-averaged sensible heat flux (Fig. 18a) is strongly modulated by the wind speed (Fig. 18b), which is greatest along and east of the q_v gradient, where the large-scale surface pressure gradient is strongest. Thus, the strongest time-averaged late morning to early afternoon sensible heating and most rapid development of the PBL does not necessarily occur over the driest soil but instead within a 100–200-km-wide SW–NE-oriented corridor near the surface q_v gradient (Fig. 14a), where winds are at least moderately strong ($|\mathbf{V}| \geq 5$ m s^{-1}) and the soil is at least moderately dry ($\leq$0.12 m^3 m^{-3}).

b. Mesoscale vertical circulations

Sensible heating is a critical factor in the growth of the PBL, with the small-scale vertical motions of the PBL themselves playing a major role in PBL growth. However, PBL growth and thermodynamic destabilization may be augmented when mesoscale ascent occurs

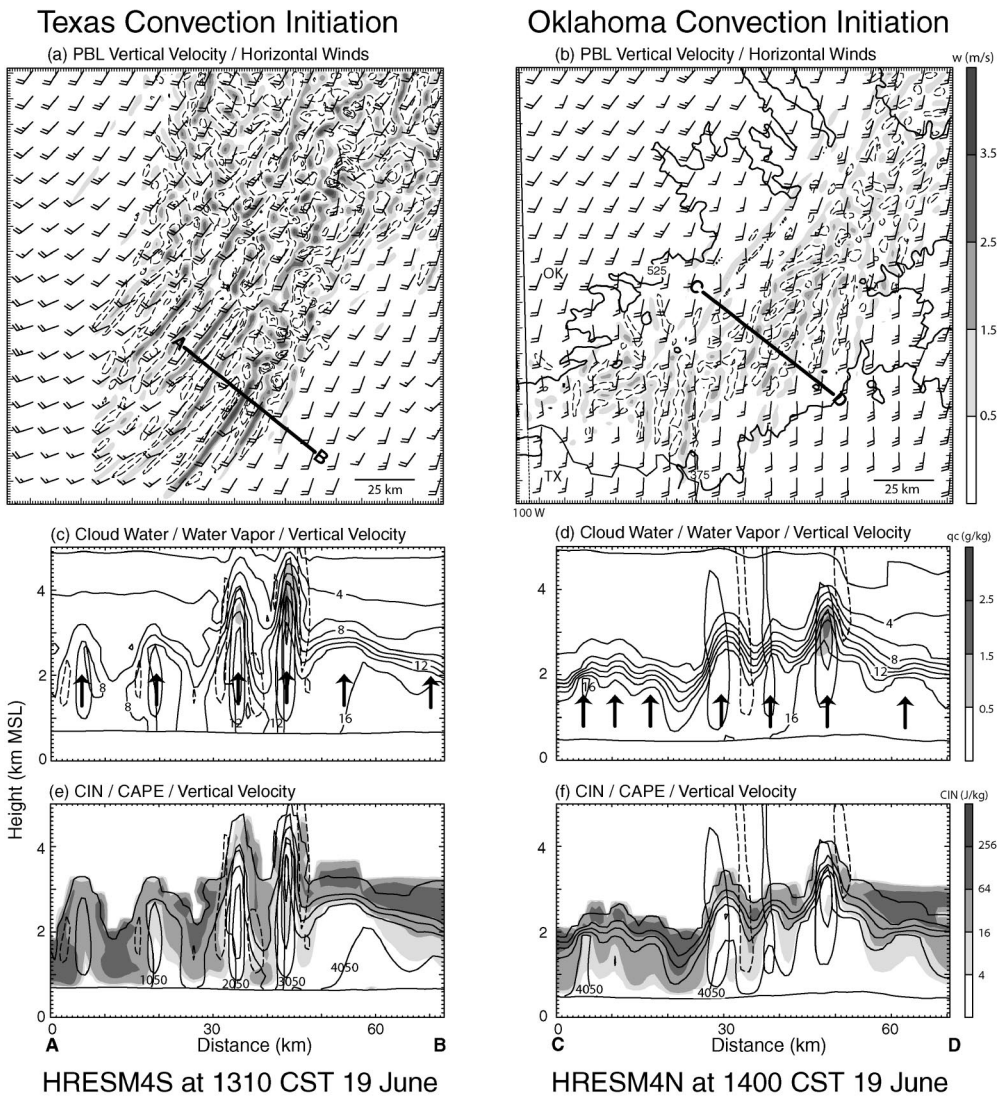

FIG. 16. PBL horizontal wind and vertical velocity (values ≥ 0.5 m s^{-1} shaded in 1 m s^{-1} intervals and values ≤ -1 m s^{-1} indicated by dashed contours with intervals of -1 m s^{-1}) for (a) the $\sigma = 0.852$ level of domain 4S (location shown in Figs. 3 and 15a) of simulation HRESM4S at 1310 CST ($t = 7.2$ h) 19 Jun 1998 and for (b) the $\sigma = 0.875$ level of domain 4N (location shown in Figs. 3 and 15a) of simulation HRESM4S at 1400 CST ($t = 8$ h) 19 Jun 1998. (b) The bold solid lines represent the 375- and 525-m terrain contours. Vertical cross sections of (c) cloud water q_c (shaded, beginning at 0.5 g kg^{-1}) and water vapor mixing ratio q_v (bold, solid contours in intervals of 2 g kg^{-1}), and vertical velocity [thin contours in intervals of 2 m s^{-1} (-2 m s^{-1}) with solid (dashed) lines beginning at 1 m s^{-1} (-1 m s^{-1})], and (e) CIN (shaded, beginning at 4 m^2 s^{-2}), CAPE (bold, solid contours in intervals of 1000 m^2 s^{-2}), and vertical velocity [as in (c)] are taken along line AB in (a) at 1310 CST. (c) The arrows indicate spacing between HCR updrafts discussed in text. (d) and (f) As in (c) and (e), respectively, but are taken along line CD in (b) at 1400 CST.

in conjunction with the strong surface heating (e.g., McGinley 1986).

In the following we examine mesoscale circulations in the vicinity of the Oklahoma portion of the q_v gradient. We focus on the Oklahoma region for the following reasons: 1) The mesoscale PBL depth maximum is particularly prominent in this location (Fig. 14); 2) intense small-scale PBL circulations that occur in this region of enhanced PBL depth are particularly critical to convection initiation, since unlike in Texas lifting along a finescale frontogenetic dryline is absent; 3) observations from the Oklahoma Mesonet exhibit a surface θ_v maximum similar to that of HRESM3 (Fig. 12), which suggests the strong likelihood of a similar maximum in PBL depth along this portion of the surface q_v gradient in the actual atmosphere.

Since the finescale grids from which the simulated deep convection initiates contain turbulent vertical cir-

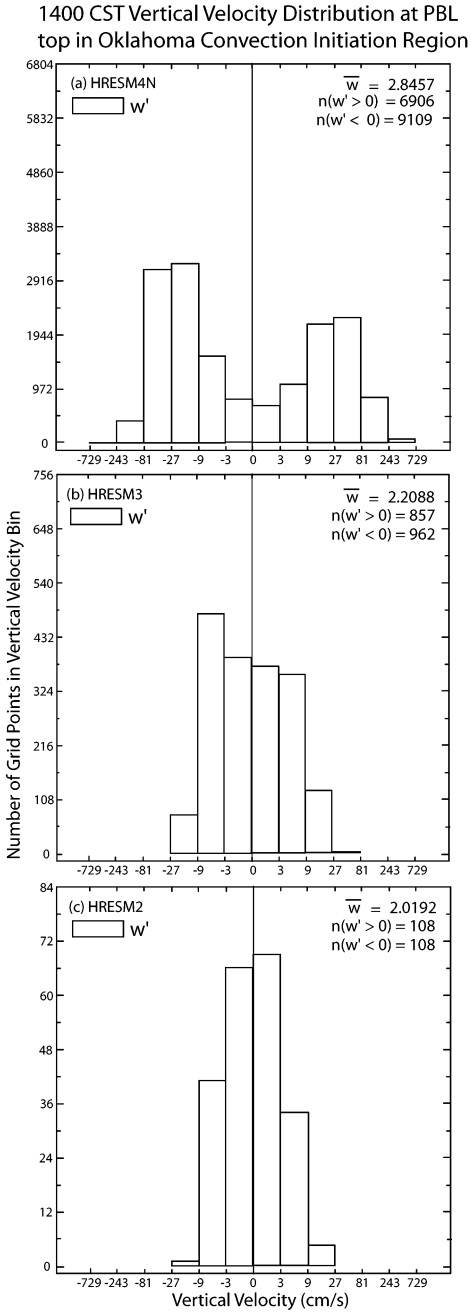

FIG. 17. 1400 CST 19 Jun 1998 PBL top vertical velocity distributions (with mean, $\overline{w}$, removed) over the area bounded by the 375- and 525-m terrain contours in Fig. 16b for the finest grids of the (a) 1.1-km (HRESM4N), (b) 3.3-km (HRESM3), and (c) 10-km (HRESM2) simulations.

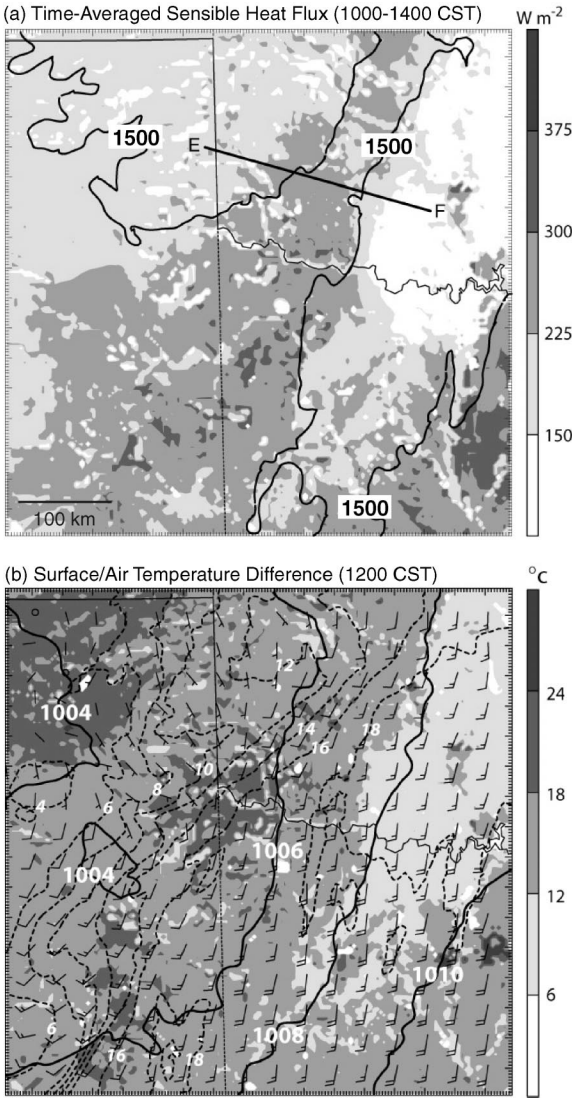

FIG. 18. (a) Time-averaged 1000–1400 CST (t = 4–8 h) surface sensible heat flux (shaded) and 1400 CST 19 Jun 1998 (t = 8 h) PBL depth (1500-m contour only; see Fig. 14a for a more complete representation) for domain 3 of simulation HRESM3. Line EF indicates the location of vertical cross sections displayed in Figs. 19 and 20. (b) 1200 CST 19 Jun 1998 (t = 6 h) temperature (°C) difference (shaded) between the ground surface and the air at the lowest model grid point located at $\sigma = 0.996$ (~25–30 m AGL), water vapor mixing ratio (dashed contours in 2 g kg^{-1} intervals) at the lowest model grid point, and sea level pressure (solid contours in 2-hPa intervals) for domain 3 of simulation HRESM3.

culations (section 4) that mask larger and more persistent mesoscale vertical circulations of lesser amplitude, we have applied a square 7 × 7 gridpoint filter to all interior points of D3 of HRESM3 and ETASM3 to investigate the occurrence of mesoscale vertical circulations and their potential importance to thermodynamic destabilization. This procedure coarsens the model output to an effective grid spacing of 23 km, which itself represents the approximate horizontal wavelength of the simulated turbulent PBL circulations on D3 (Fig. 15).

Vertical cross sections using the coarsened D3 output (Fig. 19) are constructed along line EF of Fig. 18a, which intersects the early afternoon PBL depth maximum in Oklahoma. Figures 19a and 19b reveal enhanced θ_v associated with the PBL depth maximum that develops between the early and late morning toward the

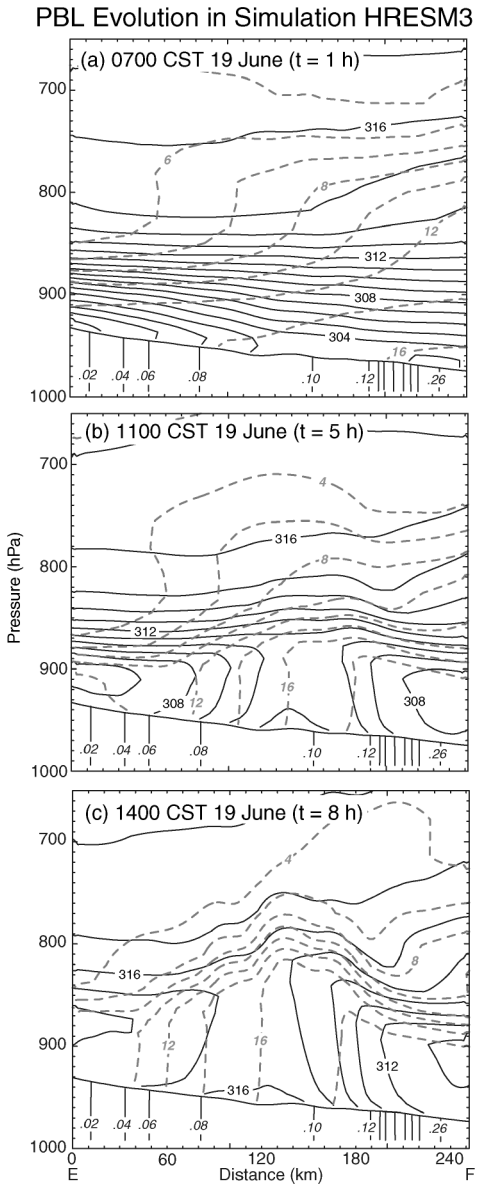

FIG. 19. Vertical structure of virtual potential temperature, θ_v (solid contours in 1-K intervals), and water vapor mixing ratio, q_v (dashed contours in 2 g kg^{-1} intervals) along line E–F of Fig. 18a within the horizontally coarsened domain 3 of simulation HRESM3 at (a) 0700 (t = 1 h), (b) 1100 (t = 5 h), and (c) 1400 (t = 8 h) CST 19 Jun 1998. The thin solid lines beneath the terrain slope of the cross section are contours of initial volumetric surface soil moisture values from domain 3 in intervals of 0.02 m^3 m^{-3}.

southeastern side of the horizontal q_v gradient near x = 140. The 1100 CST θ_v maximum with enhanced PBL depth (Fig. 19b) is situated between the initially cool region over the elevated terrain and lower elevations to the southeast, where surface θ_v increases more slowly due to weaker sensible heating (Fig. 18a) over the moister soil. The largest horizontal differences in PBL growth occur during the late morning and early afternoon. By early afternoon (1400 CST) the local maximum in PBL height has shifted westward to x = 120 (Fig. 19c) as a result of stronger heating of the dry soil in the northwest part of the cross section than over the moist soil in the southeast part.

To examine the effect of mesoscale vertical circulations on the thermodynamic stability, vertical velocity and the component of horizontal wind parallel to vertical cross-section E–F were time-averaged for a 4-h period (1000–1400 CST) prior to the onset of deep convection. Weak inflow of -1 to -2 m s^{-1} (Fig. 20a) occurs within the PBL toward the θ_v and PBL depth maxima (x = 130–150 km in Figs. 19b,c). A return branch of the horizontal flow just above the PBL is evident east of the θ_v maximum, and a ~100-km-scale region of mean ascent that is maximized with w = 5–7 cm s^{-1} at the top of the PBL (Fig. 20a) occurs near the center of the θ_v maximum (cf. Figs. 19b,c). From Fig. 20a we estimate a mean horizontal convergence of $\Delta u/\Delta x \sim 1$ m s^{-1}/20 km = 5×10^{-5} s^{-1} through the lowest km (~100 hPa) near the location of the early afternoon PBL depth maximum, which yields $w \sim 5$ cm s^{-1} at 1 km AGL. The strength of the estimated w suggests that the majority of the simulated time-averaged ascent near the top of the PBL depth maximum may be explained by the horizontal convergence in the plane of the cross section.

At location S2 where PBL-based mesoscale ascent occurs (Fig. 20a), model soundings indicate an 80-hPa increase in PBL depth from 1000 to 1400 CST (Fig. 21b). The Δp = 65-hPa vertical displacements that would arise from persistent 5 cm s^{-1} ascent at the top of the PBL during the 4-h period explains the majority of the 80-hPa increase in PBL depth. Thus the mesoscale ascent clearly augments the PBL deepening forced by sensible heating. The mesoscale updraft also acts in concert with the sensible heating to produce higher relative humidities at the top of the deepening PBL and to weaken the stable layer above the PBL (Fig. 21b). Meanwhile, the horizontal inflow branch of the circulation transports moist air from the southeast toward the mesoscale ascent region, which results in a 1.5 g kg^{-1} increase in PBL q_v (Fig. 21b) during the period of PBL growth when heating-induced vertical mixing, acting alone, would tend to decrease PBL q_v. Together, the strong sensible heating and mesoscale vertical circulation result in a mean PBL CAPE increase of 2000 m^2 s^{-2} (2600–4600 m^2 s^{-2}) and a mean PBL CIN decrease of 160 m^2 s^{-2} (170–10 m^2 s^{-2}) from 1000 to 1400 CST (Fig. 21b).

In contrast to the 80-hPa increase in PBL depth at S2 near the center of the mesoscale updraft, the PBL depth increases only 30 and 35 hPa at the locations of the flanking mesoscale downdrafts at S1 (Fig. 21a) and S3 (Fig. 21c), respectively. Significant differences in sounding evolution *above* the PBL between the mesoscale updraft and downdraft regions are also consistent with the time-averaged vertical motion pattern. For example, deep layers above the PBL experience significant (1°–2°C) warming in mesoscale downdraft regions

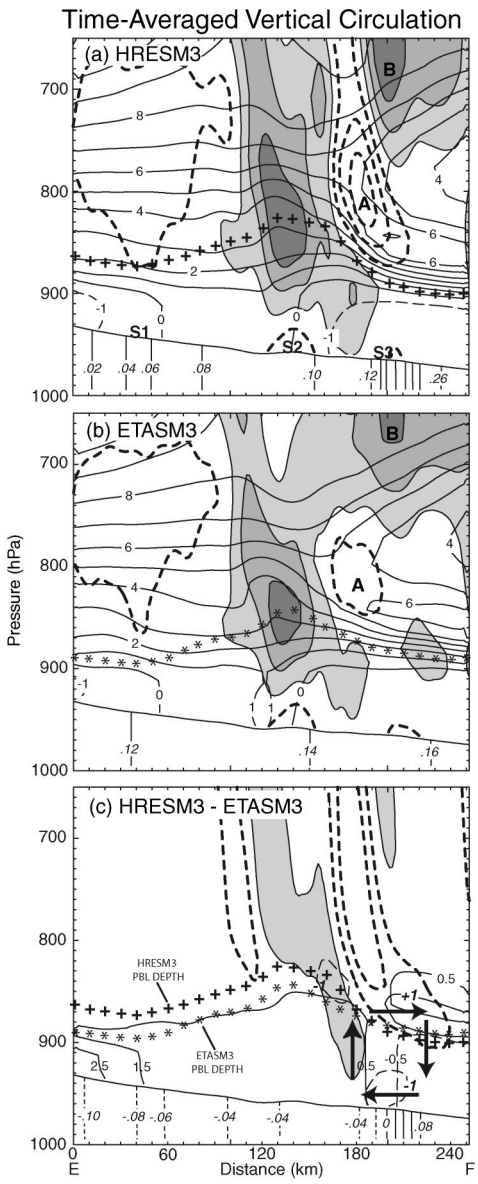

FIG. 20. (a),(b) As in Fig. 19 but with 1000–1400 CST 19 Jun 1998 (t = 4–8 h) time-averaged vertical velocity (values $\geq$ 1 cm s^{-1} shaded in intervals of 2 cm s^{-1} and values ≤ -1 cm s^{-1} contoured with bold dashed lines in intervals of -2 cm s^{-1}), horizontal wind in the plane of the cross section (thin contours in 1 m s^{-1} intervals with dashed contours indicating values $\leq$ 1 m s^{-1}, positive values indicate flow from left to right) for simulations (a) HRESM3 and (b) ETASM3, with 1400 CST (t = 8 h) PBL depth indicated by (a) the crosses in (b) the asterisks. (c) HRESM3 $-$ ETASM3 difference fields of vertical velocity (shadings and bold dashed contours), horizontal wind component in the plane of the cross section (medium contours), and initial soil moisture [as in (a) and (b)], and virtual potential temperature (thin contours in 1-K intervals). PBL vertical circulation from the difference fields is symbolically illustrated with the bold arrows. PBL depths from the individual simulations are indicated as in (a) and (b).

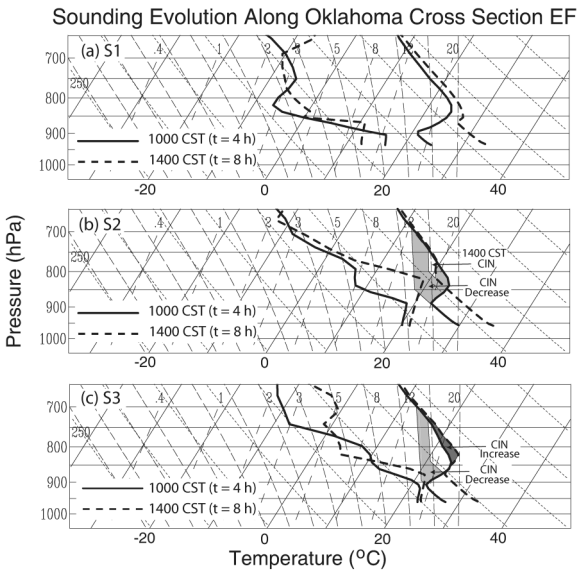

FIG. 21. Late morning to early afternoon (1000–1400 CST 19 Jun 1998) evolution of skew$T$–log$p$ profiles of lower-tropospheric temperature and moisture from the horizontally coarsened domain 3 of simulation HRESM3 at points (a) S1, (b) S2, and (c) S3 collocated with the 1000–1400 CST 19 Jun 1998 time-averaged mesoscale updraft and downdrafts along cross section EF of Fig. 20a. (b) The sum of the area of the light gray shading and the adjacent clear region approximates the 1000 CST CIN, while the clear area alone approximates the 1400 CST CIN at S2. (c) The sum of the area enclosed by the light gray shading and the adjacent clear area approximates the 1000 CST CIN as in (b), while the sum of the clear area and the area of the adjacent dark gray shading approximates the 1400 CST CIN at S3.

(Figs. 21a,c) whereas cooling occurs directly above the PBL with little temperature change above 750 hPa in the mesoscale updraft region (Fig. 21b). At S1 (Fig. 21a), collocated with the upstream downdraft (Fig. 21a), PBL drying occurring from late morning to early afternoon continues so that CAPE eventually becomes insufficient to support deep convection. In contrast, CAPE increases 1000 m^2 s^{-2} (3500–4500 m^2 s^{-2}) while CIN decreases 65 m^2 s^{-2} (145–80 m^2 s^{-2}) from 1000 to 1400 CST at S3 (Fig. 21c). However, unlike at the location of the mesoscale updraft, the CIN decrease from sensible heating at S3 is partly compensated by subsidence warming above the PBL (Fig. 21c) associated with the downstream downdraft A (Fig. 20a) and CIN is never completely removed during the afternoon in this region (cf. Fig. 13a). Note that downdraft A constitutes part of an internal gravity wave evident downstream of the region of maximum PBL depth. Examination of individual model output times (not shown) indicates that both downdraft A and updraft B (Fig. 20a) intensify in magnitude after the positive PBL depth anomaly, which arises from the differential heating and its associated mesoscale ascent, reaches sufficient amplitude to disturb the stratified fluid above the PBL.

The foregoing analysis indicates that the mesoscale vertical circulation over Oklahoma reinforces the pref-

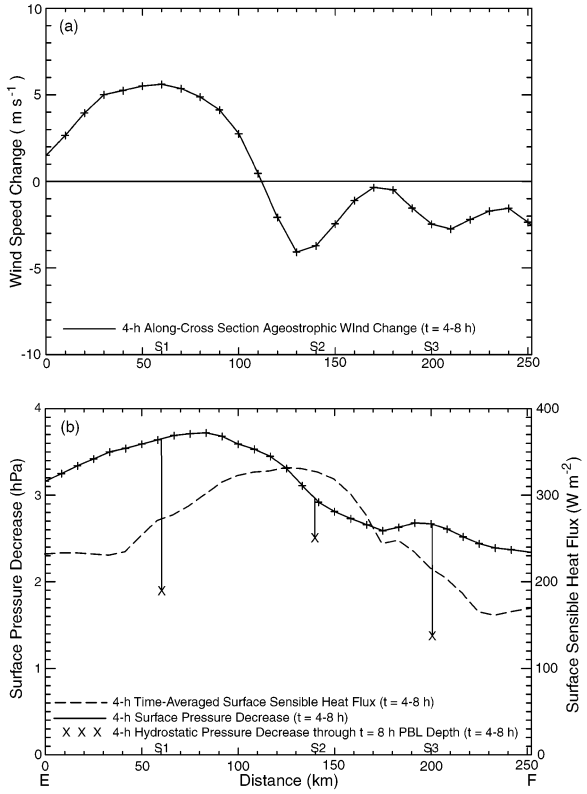

FIG. 22. (a) The 4-h change in the surface along cross-section ageostrophic wind component and (b) 4-h surface pressure decrease (solid line), 4-h surface time-averaged sensible heating (dashed line), and the 4-h hydrostatic pressure decrease through PBL depth (x symbols, see text for details) for the period from $t = 4$–8 h (1000–1400 CST 19 Jun 1998) along line EF of Fig. 18a. The annotations S1, S2, S3 refer to the locations of the lower-tropospheric mesoscale vertical velocity regions depicted in the vertical cross section along EF displayed in Fig. 20a.

erential rate of thermodynamic destabilization that begins during the morning where sensible heat flux is locally strongest. Intense finescale PBL circulations are then responsible for directly initiating deep convection (section 4) within this focused region of mesoscale ascent where CIN becomes negligible.

Given the importance of the mesoscale vertical circulation in focusing the occurrence of deep convection, we further investigate its origin. The PBL inflow from the southeast toward the region of of maximum PBL depth and mesoscale ascent (Fig. 20a) is consistent with the inland sea-breeze effect discussed in the introduction. The inland sea-breeze mechanism requires a differential lowering of pressure along the terrain slope, which is a hydrostatic consequence of differential sensible heat flux and the associated differential growth of the PBL (Fig. 18a). This mechanism promotes horizontal convergence and lower-tropospheric ascent associated with the ageostrophic flow response to the intensifying surface pressure gradient.

Figure 22a indicates an increase in downslope (upslope) surface ageostrophic flow in the northwestern (southeastern) part of cross-section EF from 1000 to 1400 CST, during which the PBL depth maximum (Fig. 19) and the mesoscale ascent (Fig. 20a) becomes well established. This evolution in surface ageostrophic flow is generally consistent with the 4-h surface pressure decreases (Fig. 22b), which support generation of a surface isallobaric horizontal wind component, as $\partial u_{ag}/\partial t$ is predominately positive (negative) at cross-section locations where $\partial/\partial x$ ($\partial p/\partial t$) is negative (positive).

To illustrate the association of surface pressure changes with surface heating, PBL depth, and effects of the mesoscale vertical circulation, we estimate the 4-h hydrostatic surface pressure change ΔP due to warming through a surface-based column of depth ΔZ using

$$\Delta P = p_{sf}\left[1 - \exp\left(\frac{-g\Delta Z}{R\overline{T}_{vf}}\right)\right] - p_{si}\left[1 - \exp\left(\frac{-g\Delta Z}{R\overline{T}_{vi}}\right)\right], \quad (3)$$

derived from an approximate vertical integration of the hypsometric equation (e.g., Holton 1992, p. 20). In (3), ΔZ is the local depth of the 1400 CST PBL, p_{si} and p_{sf} are the surface pressures at 1000 and 1400 CST, respectively, and $\overline{T}_{vi}$ and $\overline{T}_{vf}$ are the mean virtual temperatures of the column at 1000 and 1400 CST, respectively. At $x = 140$ km, near the location of the maximum time-averaged sensible heating, using ΔZ of 1380 m and $\overline{T}_{vi} = 299.9$ K and $\overline{T}_{vf} = 304.8$ K in (3) yields a 2.5-hPa surface pressure decrease, which reasonably approximates the simulated 2.9-hPa surface pressure decrease (Fig. 22b) from $p_{si} = 956.2$ hPa to $p_{sf} = 953.3$ hPa. In contrast, both northwest (at $x = 60$ km) and southeast (at $x = 200$ km) of the location of maximum sensible heating, where subsidence warming occurs through a deep layer above the PBL (Figs. 21a,c), the estimated pressure decreases based solely on the local warming and deepening of the PBL are 1.9 and 1.4 hPa, respectively, accounting for only 55% of the simulated 3.5- and 2.6-hPa decreases at these locations (Fig. 22b).

The analysis just presented points to the following sequence of events. Differential heating along the sloping terrain of differing soil moisture results in a localized region of maximum surface pressure falls. This, in turn, generates a mesoscale vertical circulation that further alters the pressure field through its associated adiabatic temperature changes above the PBL (Fig. 21). This effect of the circulation itself on the pattern of surface pressure decreases is evident by the ~50-km northwestward shift of the location of maximum surface pressure falls from that of the maximum surface sensible heating (Fig. 22b) for this 4-h period during which the mesoscale vertical circulation becomes well established (Fig. 20a).

c. Influence of soil moisture initialization

Significant differences in the strength of the time-averaged mesoscale circulation between the identically coarsened HRESM3 (Fig. 20a) and ETASM3 (Fig. 20b) simulations are restricted to the region east of the PBL depth maximum. Here, a circulation is also evident in the HRESM3 − ETASM3 difference fields (Fig. 20c) and is centered on an enhanced horizontal gradient of the differenced PBL θ_v, which is associated with the more intense soil moisture gradients in HRESM3 near $x = 200$ (cf. Figs. 20a,b) that result in more intense localized horizontal gradients of sensible heating in this simulation. However, similarities in both the location of the PBL depth maxima and the magnitude of the accompanying mesoscale ascent to the west (near $x = 140$) between HRESM3 and ETASM3 (Figs. 20a,b) suggests the broader soil moisture variations along the sloping terrain, apparent in both HRESM3 and ETASM3, may be more important to the overall development of the mesoscale vertical circulation in SW Oklahoma than the more localized, stronger soil moisture gradients located farther east in HRESM3. The similarity in the location of the maximum PBL depth and the strength of the accompanying maximum in mesoscale ascent between HRESM3 and ETASM3 are consistent with a similar timing, location and character of convection initiation over Oklahoma (Figs. 6a,b and 15a,b).

As noted earlier, the most significant differences in convection initiation and subsequent 1500–1800 CST precipitation pattern between HRESM3 (Fig. 6a) and ETASM3 (Fig. 6b) occur over Texas, where activity is more extensive both along and up to ~100 km east of the dryline in HRESM3. The eastern edge of the convection occurs a few tens of kilometers farther east in ETASM3 and precedes the widely scattered convection near the dryline (Fig. 15b). This sequence of events contrasts with the situation in HRESM3, where convection begins at the dryline (Fig. 15a) and then progresses eastward.

Time-averaged sensible heat flux from 1000 to 1400 CST is generally larger in HRESM3 (Fig. 23a) than in ETASM3 (Fig. 23b) over a region extending from 100 km west to 100 km east of the Texas dryline. This is consistent with a deeper early afternoon PBL (Fig. 14) and more energetic PBL vertical motions (Fig. 15) in the early to midafternoon near the Texas dryline in HRESM3. Well east of the dryline, where the band of deep convection develops in ETASM3 (Fig. 6b), the magnitude of the sensible heating in ETASM3 is, however, comparable to that in HRESM3 (Fig. 23).

The most significant difference between the 1500 CST ETASM3 and HRESM3 soundings in the vicinity of the ETASM3 convective band is a ~20-hPa deeper PBL in ETASM3 (Fig. 24a). The greater PBL depth, despite slightly cooler and moister mean PBL conditions, is suggestive of enhanced lower-tropospheric ascent in ETASM3, consistent with the more pronounced

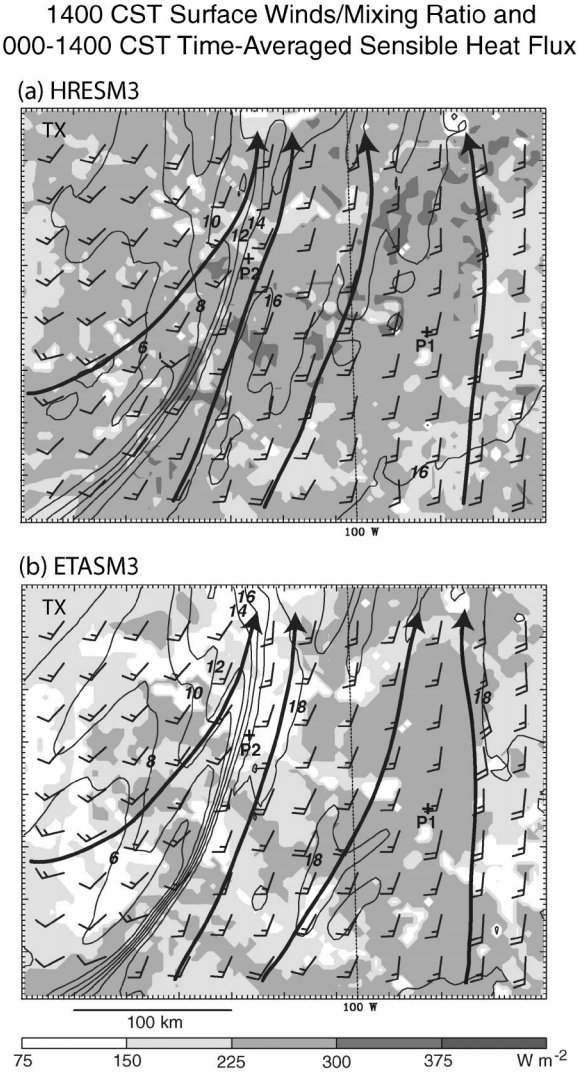

FIG. 23. 1000–1400 CST 19 Jun 1998 (t = 4–8 h) time-averaged surface sensible heat flux (shadings in 75 W m^{-2} intervals beginning at 150 W m^{-2}), and 1400 CST 19 Jun (t = 8 h) horizontal winds and water vapor mixing ratio (contoured in 2 g kg^{-1} intervals) at the lowest model grid point (σ = 0.996, ~25–30 m AGL) for a subset of domain 3 of simulations (a) HRESM3, and (b) ETASM3. Bold lines with arrowheads depict selected streamlines. Here, P1 and P2 refer to the locations of soundings displayed in Fig. 24.

mesoscale surface confluence/convergence zone in the vicinity of P1 in ETASM3 (Fig. 23b). The reasons for the differences in the mesoscale surface flow pattern are not entirely clear but could be a manifestation of the more concentrated sensible heat flux maximum east of the dryline in ETASM3 (Fig. 23), which appears to be of sufficient horizontal scale and continuity to drive a weak mesoscale circulation (e.g., Segal and Arritt 1992).

Soil moisture differences between the two simulations (Figs. 4a,b) are much greater in the vicinity of the dryline near P2 (ETASM3 − HRESM3 ~ 0.10 m^3 m^{-3}) than east of the dryline near P1 (ETASM3 − HRESM3 ~ 0.01 m^3 m^{-3}). As a result, greater sensible heat fluxes

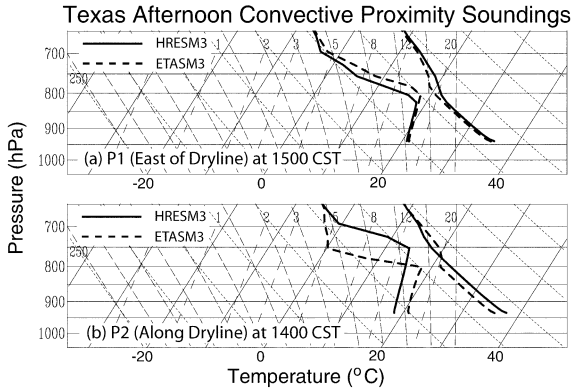

FIG. 24. Afternoon skew$T$–log$p$ profiles of temperature and moisture from the domain 3 locations of (a) P1 and (b) P2 displayed in Figs. 4 and 23 prior to local development of afternoon convection.

near the dryline in HRESM3 (Fig. 23a) than in ETASM3 (Fig. 23b), contribute to a ~50-hPa deeper early afternoon PBL in HRESM3 (Fig. 24b). Confluent surface flow occurs in the vicinity of the dryline in both simulations (Fig. 23). However, unlike in HRESM3, the sensible heating in ETASM3 is insufficient to deepen the PBL and remove stability above it to an extent that permits widespread dryline convection (cf. Figs. 6a,b).

Our finding of greater efficacy in triggering deep convection over relatively dry soil when more net radiation is partitioned into sensible heat flux is consistent with the one-dimensional modeling results of Findell and Eltahir (2003). Those authors note that the dry-soil advantage over regimes like the dryline environment results primarily from steep lapse rates above the early morning PBL in this region. Over other continental locations, where conditions above the PBL are more statically stable with higher relative humidities, they find that wetter soils are more conducive to convection initiation. Our analysis further emphasizes that characteristics of the initial soil moisture distribution, including both its local value and horizontal variability, can significantly influence convection initiation through its effect on the subsequent thermodynamic stability and lower-tropospheric convergence, even in cases where soil moisture differences among simulations are insufficient to significantly influence dryline development itself.

6. Summary and discussion

This study has reported results from simulations of the evolution of a southern Great Plains (SGP) moisture gradient and its associated afternoon convection initiation. The simulations were conducted with a convection-resolving mesoscale model, initialized using a high-resolution land surface data assimilation system (HRLDAS). The initialization time coincided with the beginning of a multiday period during which deep, moist convection initiated each day during the mid-to-late afternoon either along or near a diurnally varying but otherwise quasi-stationary dryline. Relatively weak synoptic forcing allowed us to more easily isolate the role of land surface–lower-tropospheric interactions on the evolution of the q_v gradient and its association with convection initiation during a representative daytime diurnal cycle.

A diagnostic analysis established the importance of multiple scales of motion on convection initiation. A ~100-km-wide late morning to early afternoon zone of enhanced PBL depth, oriented along a surface moisture gradient of variable strength from southwest Texas into north-central Oklahoma, contained finescale ($L \sim 10$ km) PBL circulations that initiated deep convection. The mesoscale zone of enhanced PBL depth was particularly crucial to the simulated convection initiation over Oklahoma, where an intense and localized surface dryline did not occur. In this region the mesoscale zone of preferential PBL deepening was initiated by differential sensible heating over sloped terrain of differing soil moisture. The differential sensible heating forced a mesoscale vertical circulation, which reinforced the differential PBL deepening and thermodynamic destabilization, and helped govern the horizontal scale within which more intense finescale circulations that directly initiated deep convection occurred.

The simulations showed significant sensitivity of the location and areal coverage of convection initiation to details of the soil moisture initialization. A control simulation that used a finescale initial soil moisture field obtained from HRLDAS accurately captured the timing and location of the observed convection initiation. In a sensitivity simulation that used a coarser initial soil moisture representation, typical of those currently in use in operational NWP models, the location of the forecast convection initiation was significantly less accurate over a portion of the model domain despite a forecast of dryline structure and evolution that was broadly similar to that of the control simulation. The differences in the two forecasts of convection initiation are attributed to subtle differences in the lower-tropospheric thermodynamic structure that appear to have originated from localized differences in the partitioning between surface sensible and latent heat fluxes.

As grid resolution continues to improve in operational NWP models, the finding of an improved forecast of convection initiation using a more detailed and accurate initialization of soil moisture has potentially important implications for operational forecasts of convection initiation over the SGP and other locations. Additional studies are required that examine the extent to which the results from the current simulations may be relevant to additional cases of convection initiation occurring in different synoptic environments.

The numerical simulations discussed in this paper compare favorably with available observations. For example, similar evolution of model surface data and vertical thermodynamic profiles with those determined from data analysis of the NWS conventional observing

network and the Oklahoma mesonet suggests that the model is handling the daytime diurnal cycle of the PBL, which impacts both dryline evolution and convection initiation, in a realistic fashion. Moreover, the mode of simulated afternoon convection initiation from elongated PBL circulations compares favorably with that inferred from visible satellite observations, which indicate a qualitatively similar eruption of deep convection from within a midafternoon zone of cumulus cloud streets of comparable width that was similarly aligned along the axis of the moisture gradient zone.

Unfortunately, many of the important details of the simulated dryline evolution and convection initiation process cannot be confirmed with the available data, which represents a shortcoming of the current study. The recently completed field phase of the International H_2O Project (IHOP; Weckwerth et al. 2004) was designed to examine finescale water vapor variability, boundary layer processes and convection initiation over the SGP. More detailed measurements from IHOP than heretofore available provide an excellent opportunity to potentially confirm and better understand aspects of dryline evolution and convection initiation suggested by the current simulations and to motivate future diagnostic studies.

Acknowledgments. The authors acknowledge Tom Warner (NCAR/University of Colorado) for useful discussions regarding this research and David Ahijevych (NCAR) for his aid in the productions of Figures 7 and 21. The authors are also grateful to Chris Davis, Peggy LeMone, and Tammy Weckwerth (each of NCAR) for their informal reviews and to Lewis Grasso (CIRA/Colorado State University) who provided an AMS journal review. Each of these reviews led to significant impovements in this manuscript. This research was supported by United States Weather Research Program (USWRP) Grant Contract NSF 01 and the NCAR Water Cycle Initiative.

REFERENCES

Anthes, R. A., Y.-H. Kuo, S. G. Benjamin, and Y.-F. Li, 1982: The evolution of the mesoscale environment of severe local storms: Preliminary modeling results. *Mon. Wea. Rev.,* **110,** 1185–1213.

Atkins, N. T., R. M. Wakimoto, and C. L. Ziegler, 1998: Observations of finescale structure of a dryline during VORTEX 95. *Mon. Wea. Rev.,* **126,** 525–550.

Benjamin, S. G., 1986: Some effects of surface heating and topography on the regional severe storm environment. Part II: Two-dimensional idealized experiments. *Mon. Wea. Rev.,* **114,** 330–343.

——, and T. N. Carlson, 1986: Some effects of surface heating and topography on the regional severe storm environment. Part I: Three-dimensional simulations. *Mon. Wea. Rev.,* **114,** 307–329.

——, G. A. Grell, J. M. Brown, and T. G. Smirnova, 2004a: Mesoscale weather prediction with the RUC hybrid isentropic–terrain-following coordinate model. *Mon. Wea. Rev.,* **132,** 473–494.

——, and Coauthors, 2004b: An hourly assimilation–forecast cycle: The RUC. *Mon. Wea. Rev.,* **132,** 495–518.

Brock, F. V., K. C. Crawford, R. L. Elliott, G. W. Cuperus, S. J. Stadler, H. L. Johnson, and M. D. Eilts, 1995: The Oklahoma Mesonet: A technical overview. *J. Atmos. Oceanic Technol.,* **12,** 5–19.

Chen, F., and J. Dudhia, 2001: Coupling an advanced land surface–hydrology model with the Penn State–NCAR MM5 modeling system. Part I: Model implementation and sensitivity. *Mon. Wea. Rev.,* **129,** 569–585.

——, Z. Janjic, and K. Mitchell, 1997: Impact of atmospheric surface-layer parameterizations in the new land-surface scheme of the NCEP mesoscale ETA model. *Bound.-Layer Meteor.,* **70,** 391–421.

——, T. T. Warner, and K. Manning, 2001: Sensitivity of orographic moist convection to landscape variability: A study of the Buffalo Creek, Colorado, flash flood case of 1996. *J. Atmos. Sci.,* **58,** 3204–3223.

——, K. W. Manning, D. N. Yates, M. A. LeMone, S. B. Trier, R. Cuenca, and D. Niyogi, 2004: Development of a High Resolution Land Data Assimilation System (HRLDAS). Preprints, *16th Conf. on Numerical Weather Prediction,* Seattle, WA, Amer. Meteor. Soc., CD-ROM, 22.3.

Colby, F. P., Jr., 1984: Convective inhibition as a predictor of convection during AVE-SESAME II. *Mon. Wea. Rev.,* **112,** 2239–2252.

Doswell, C. A., III, and E. N. Rasmussen, 1994: The effect of neglecting the virtual temperature correction on CAPE calculations. *Wea. Forecasting,* **9,** 625–629.

Dudhia, J., 1989: Numerical study of convection observed during the winter monsoon experiment using a mesoscale two-dimensional model. *J. Atmos. Sci.,* **46,** 3077–3107.

Etling, D., and R. A. Brown, 1993: Roll vortices in the planetary boundary layer: A review. *Bound.-Layer Meteor.,* **65,** 215–248.

Findell, K. L., and E. A. B. Eltahir, 2003: Atmospheric controls on soil moisture–boundary layer interactions. Part II: Feedbacks within the continental United States. *J. Hydrometeor.,* **4,** 570–583.

Fulton, R. A., J. P. Breidenbach, D.-J. Seo, D. A. Miller, and T. O'Bannon, 1998: The WSR-88D rainfall algorithm. *Wea. Forecasting,* **13,** 377–395.

Grasso, L. D., 2000: A numerical simulation of dryline sensitivity to soil moisture. *Mon. Wea. Rev.,* **128,** 2816–2834.

Grell, G. A., 1993: Prognostic evaluation of assumptions used by cumulus parameterizations. *Mon. Wea. Rev.,* **121,** 764–787.

——, J. Dudhia, and D. R. Stauffer, 1994: A description of the fifth generation Penn State/NCAR mesoscale model (MM5). NCAR Tech. Note NCAR/TN 398+STR, 138 pp.

Hane, C. E., H. B. Bluestein, T. M. Crawford, M. E. Baldwin, and R. M. Rabin, 1997: Severe thunderstorm development in relation to along-dryline variability: A case study. *Mon. Wea. Rev.,* **125,** 231–251.

Holton, J. R., 1992: *An Introduction to Dynamic Meteorology.* 3d ed. Academic Press, 511 pp.

Jacquemin, B., and J. Noilhan, 1990: Sensitivity study and validation of a land surface parameterization using the HAPEX-MOBILHY data set. *Bound.-Layer Meteor.,* **52,** 93–124.

Janjic, Z. I., 1990: The step-mountain coordinate: Physical package. *Mon. Wea. Rev.,* **118,** 1429–1443.

——, 1994: The step-mountain eta coordinate: Further development of the convection, viscous sublayer, and turbulent closure schemes. *Mon. Wea. Rev.,* **122,** 927–945.

Lanicci, J. M., T. N. Carlson, and T. T. Warner, 1987: Sensitivity of the Great Plains severe-storm environment to soil moisture distribution. *Mon. Wea. Rev.,* **115,** 2660–2673.

LeMone, M. A., 1973: The structure and dynamics of horizontal roll vortices in the planetary boundary layer. *J. Atmos. Sci.,* **30,** 1077–1091.

McCarthy, J., and S. E. Koch, 1982: The evolution of an Oklahoma dryline. Part I: A meso- and subsynoptic-scale analysis. *J. Atmos. Sci.,* **39,** 225–236.

McGinley, J., 1986: Nowcasting mesoscale phenomena. *Mesoscale*

Meteorology and Forecasting, P. S. Ray, Ed., Amer. Meteor. Soc., 657–688.

McGuire, E. L., 1962: The vertical structure of three drylines as revealed by aircraft traverses. National Severe Storms Project Rep. 7.

Miller, J. A., T. A. Kovacs, and P. R. Bannon, 2001: A shallow water model of the diurnal dryline. *J. Atmos. Sci.,* **58,** 3508–3524.

Ogura, Y., and Y. L. Chen, 1977: Life history of an intense mesoscale convective storm in Oklahoma. *J. Atmos. Sci.*, **34,** 1458–1476.

Pan, H.-L., and L. Mahrt, 1987: Interaction between soil hydrology and boundary-layer development. *Bound.-Layer Meteor.*, **38,** 185–202.

Parsons, D. B., M. A. Shapiro, R. M. Hardesty, R. J. Zamora, and J. M. Intrieri, 1991: The fine-scale structure of a west Texas dryline. *Mon. Wea. Rev.*, **119,** 1242–1258.

——, ——, and E. Miller, 2000: The mesoscale structure of a nocturnal dryline and of a frontal–dryline merger. *Mon. Wea. Rev.*, **128,** 3824–3838.

Peckham, S. E., and L. J. Wicker, 2000: The influence of topography and lower-tropospheric winds on dryline morphology. *Mon. Wea. Rev.,* **128,** 2165–2189.

Pielke, R. A., Sr., 2001: Influence of the spatial distribution of vegetation and soils on the prediction of cumulus convective rainfall. *Rev. Geophys.*, **39,** 151–177.

——, and M. Segal, 1986: Mesoscale circulations forced by differential terrain heating. *Mesoscale Meteorology and Forecasting*, P. S. Ray, Ed., Amer. Meteor. Soc., 516–548.

Pinker, R. T., I. Laszlo, J. D. Tarpley, and K. Mitchell, 2002: Geostationary satellite products for surface energy balance models. *Adv. Space Res.*, **30,** 2427–2432.

Reisner, J., R. J. Rasmussen, and R. T. Bruintjes, 1998: Explicit forecasting of supercooled liquid water in winter storms using the MM5 mesoscale model. *Quart. J. Roy. Meteor. Soc.*, **124B,** 1071–1107.

Rhea, J. O., 1966: A study of thunderstorm formation along dry lines. *J. Appl. Meteor.,* **5,** 58–83.

Schaake, J. C., V. I. Koren, Q. Y. Duan, K. Mitchell, and F. Chen, 1996: A simple water balance runoff model (SWB) for estimating runoff at different spatial and temporal scales. *J. Geophys. Res.*, **101,** 7461–7475.

Schaefer, J. T., 1974: A simulative model of dryline motion. *J. Atmos. Sci.,* **31,** 956–964.

Segal, M., and R. W. Arritt, 1992: Nonclassical mesoscale circulations caused by sensible heat-flux gradients. *Bull. Amer. Meteor. Soc.*, **73,** 1593–1604.

Shaw, B. L., R. A. Pielke, and C. L. Ziegler, 1997: A three-dimensional simulation of a Great Plains dryline. *Mon. Wea. Rev.*, **125,** 1489–1506.

Stull, R. B., 1988: *An Introduction to Boundary Layer Meteorology*. Kluwer Academic, 666 pp.

Sun, W.-Y., and Y. Ogura, 1979: Boundary-layer forcing as a possible trigger to squall-line formation. *J. Atmos. Sci.*, **36,** 235–254.

——, and C.-C. Wu, 1992: Formation and diurnal variation of the dryline. *J. Atmos. Sci.,* **49,** 1606–1619.

Weckwerth, T. M., J. W. Wilson, and R. M. Wakimoto, 1996: Thermodynamic variability within the convective boundary layer due to horizontal convective rolls. *Mon. Wea. Rev.*, **124,** 769–784.

——, and Coauthors, 2004: Overview of the International H_2O Project (IHOP 2002) and some preliminary highlights. *Bull. Amer. Meteor. Soc.,* **85,** 253–277.

Ziegler, C. L., and E. N. Rasmussen, 1998: The initiation of moist convection at the dryline: Forecasting issues from a case study perspective. *Wea. Forecasting*, **13,** 1106–1131.

——, W. J. Martin, R. A. Pielke, and R. L. Walko, 1995: A modeling study of the dryline. *J. Atmos. Sci.*, **52,** 263–285.

——, T. J. Lee, and R. A. Pielke, 1997: Convective initiation at the dryline: A modeling study. *Mon. Wea. Rev.*, **125,** 1001–1026.

Zilitinkevich, S., 1995: Non-local turbulent transport: Pollution dispersion aspects of coherent structure of convective flows. *Air Pollution Theory and Simulation*, H. Power, N. Moussiopoulos, and C. A. Brebbia, Eds., *Air Pollution III*, Vol. I, Computational Mechanics Publications, 53–60.